

Literature Survey

Distributed wavefront reconstruction for large Adaptive Optics systems

João Silva

Literature Survey

Literature Survey

Distributed wavefront reconstruction for large Adaptive Optics systems

LITERATURE SURVEY

João Silva

February 1, 2014

Abstract

This is an abstract.

Contents

Preface	ix
Acknowledgements	xi
1 Introduction	1
1-1 Nomenclature	2
2 Adaptive Optics: an overview	5
2-1 The Adaptive Optics Control Problem	5
2-2 Wavefront sensors	7
2-2-1 Focal spot deviation	7
2-2-2 Shack-Hartmann sensor	8
2-3 Wavefront reconstruction	10
2-3-1 Zonal Reconstruction	10
2-3-2 Modal Reconstruction	11
2-3-3 Novel methods for wavefront reconstruction	12
2-4 Closed loop control with Deformable Mirror	15
2-4-1 Classical approach	15
2-4-2 Distributed approach	16
3 B-Splines framework	17
4 Distributed Optimization	21
4-1 Primal Decomposition	21
4-2 Dual Ascent	22
4-2-1 Dual Decomposition	23
4-2-2 Method of Multipliers	24
4-3 ADMM	24
4-3-1 Exchange problem	25

5	Results	27
5-1	Intensity-based reconstruction using B-Splines	27
5-1-1	Wavefront Reconstruction	28
5-1-2	Simulation Results	32
5-1-3	Conclusions	34
5-2	Compressive sampling using Jacobian analysis	35
5-2-1	Acceleration study through compressive sampling	36
5-2-2	Numerical Simulations	37
5-2-3	Conclusion	40
5-3	Distributed methods	40
5-3-1	Separable problem formulation	40
5-3-2	ADMM application to wavefront reconstruction	43
5-3-3	Further improvements	43
5-3-4	Results	44
6	Thesis Goal and Research Approach	45
6-1	Thesis Goal	45
6-2	Research Approach	45
A	Model of the Shack-Hartmann Wavefront Sensor	47
A-1	Intensity Distribution model	47
A-2	Slope model	49
B	Auxiliar derivations to support ADMM method	51
	Bibliography	53
	Glossary	59
	List of Acronyms	59
	List of Symbols	59

List of Figures

2-1	Schematic representation of an AO system, and its main components.	6
2-2	Airy Disk	7
2-3	Schematic of an Hartmann array of pupils (or apertures). (source: "Hartmann Wavefront Analyzer Tutorial, Spiricon Laser Beam Diagnostics")	8
2-4	1 dimensional representation of a Shack-Hartmann sensor. (source: Lecture notes on Control for High Resolution Imaging)	9
2-5	Phase points (denoted with a circle) and slopes (denoted with a dash) used by (Left and center) Hudgin and (Right) Fried (image retrieved from [1])	11
2-6	Block diagram of a classical feedback loop used in Adaptive Optics	16
3-1	IMAGE OF A B-NET	19
5-1	Close-up on one of the subapertures. In the left (right) subaperture a type I (II) triangulation was defined using 2 (4) simplices per subaperture	31
5-2	(a) Reconstructed phase distribution for $\alpha_4 = 0.1\lambda$ and (b) its error (both normalized to the wavelength λ) when the intensity distribution was subject to noise ($\sigma = 4 \times 10^{-4}$)	33
5-3	Comparison of the RMS of the wavefront reconstruction between the new spline based WFR method and the modal reconstruction method (in open-loop). It is clear that due to the influence of the noisy measurements the RMS values reach a threshold when the aberrations get smaller: around $1.5 \times 10^{-3}\lambda$ for modal reconstruction and $2.5 \times 10^{-4}\lambda$ for spline-based reconstruction. Other experiments were done with different incoming wavefronts and the results were similar to the one presented above.	34
5-4	Simplified representation of a feedback loop used in Adaptive Optics	35
5-5	RMS error evolution for a classical AO setup comparing the modal and the spline-based reconstruction method.	35
5-6	RMS errors between the reconstructed and the original 4th order Zernike wavefront for decreasing percentage $cr\%$ of intensity measurements used. Triangles: Randomly computed selection matrix. Circles: Jacobian based selection matrix. Crosses: Real time computational complexity depending on $cr\%$	38

- 5-7 RMS errors for different reconstruction methods: Spline based method for 10% of the intensity measurements (Triangles), spline based method using all given intensity measurements (Squares), classical modal reconstruction method for slope measurements (Stars). Top: Fix noise standard deviation $\sigma_{\text{ccd}} = 4 \times 10^{-4}$, increasing aberration strength simulated by augmenting the Zernike coefficient α_4 . Bottom: Fix astigmatic aberration for $\alpha_4 = 0.1\lambda$, noise with varying standard deviation σ_{ccd} 41
- 5-8 RMS value of the residual wavefront for a classical closed loop AO setup for reconstruction from intensities with the spline based method (Solid: 10% of pixels; Dashed: all pixels) and from slopes with the classical modal method (Dot-dashed). 42

List of Tables

5-1	Wavefront reconstruction RMS errors normalized to the wavelength average over 5 different noise distributions. Both the dual ascent in D-SABRE and the ADMM implementation were run for 500 iterations with no stopping criterion	44
-----	---	----

Preface

The graduation project in which this Literature Survey is included appears as a natural follow-up after concluding a small project in the last quarters of 2012/2013 under the supervision of Prof. dr. ir. Michel Verhaegen. The main purpose of that project was to develop a more accurate and distributable algorithm to reconstruct the phase distribution.

When the project was concluded both Prof. Verhaegen and myself showed interest in continuing the work already initiated. My motivation was two-fold: on the one hand, I enjoyed working in a multidisciplinary environment in a subject which was not very familiar to me and embedded in a team which was always both demanding and supportive. On the other hand, it would give me the opportunity of working in distributed optimization and of learning GPU programming, which are two subjects of great interest to me.

Although the results are not that many at this stage I would like to thank Elisabeth Brunner for her constant support and willingness to discuss my (technical) problems, Alessandro Polo for the patience in explaining me the most basic Optics concepts and Prof. Verhaegen for his vision in coming up with this solution and for the motivation and excitement that he transmits.

Acknowledgements

I would like to thank my supervisor for his assistance during the writing of this thesis...

By the way, it might make sense to combine the Preface and the Acknowledgements. This is just a matter of taste, of course.

Delft, University of Technology
February 1, 2014

João Silva

“In the future, airplanes will be flown by a dog and a pilot. And the dog’s job will be to make sure that if the pilot tries to touch any of the buttons, the dog bites him.”

— *Scott Adams*

Chapter 1

Introduction

We are currently being presented an increasingly amount of challenges in the area of photonics as more and more applications in need for active "photon control" sprout in different fields of science. In this survey, the main focus is on the field of Adaptive Optics (AO) which involves measuring, reconstructing and reshaping the phase of a photon wavefront in real-time. More specifically, the measurement phase involves a wavefront sensor which gives us some information regarding the wavefront. Then, using that data the phase of the wavefront is retrieved. Finally, an actuated device, such as a deformable mirror, is used to reshape the phase of the wavefront in real-time.

Although AO may seem like a very specific topic, there are a large number of real-time applications in this field.

AO was first developed with military purposes. Using segmented mirrors to compensate for the effects of the atmosphere, scientists were able to obtain a larger signal intensity from laser beams that were used for telecommunication purposes [2].

In astronomy, AO is also used to counteract the effect of the turbulence in the atmosphere which blurs the images that arrive at ground-based telescopes. When it was applied to these telescopes for the first time, the quality of the images rivalled that of the Hubble Space telescope [2]. The current efforts are mainly directed to enhance the performance of the next-generation of ground-based telescopes. One of those telescopes is the European Extremely Large Telescope (E-ELT). This telescope will, by construction, have a very large collecting area which will, by itself, acquire a larger amount of astronomical data. Moreover, due to the integration of Adaptive Optics from the beginning of the design plans, the spatial resolution can be increased up to one order of magnitude compared to the state-of-the art telescopes [3].

Adaptive optics also has its uses for Integrated Circuit manufacturing. Extreme Ultraviolet Lithography (EUVL), which is a promising next-generation method of circuit printing, must have a very high precision such that the doping of the semiconductor is done correctly. AO could be used to correct deformations that exist in the mirrors that perform part of the circuit printing which are very susceptible to heat deformation. Although there are no articles with

a complete AO setup for this application, some authors have shown some promising results regarding the phase retrieval phase [4, 5].

In confocal and multi-photon microscopes, which are able to produce three-dimensional images of volumetric objects, the resolution of the images is severely affected by the changes in the refractive index of the object in question. These aberrations can be minimized by using AO similarly to what is done in astronomy where one possible source of the aberrations is the change in refractive index of the atmosphere.

In retinal imaging, it is worth mentioning two methods that have immensely improved the way scientists and physicians perceive the eye. Those methods are Scanning Laser Ophthalmoscopy and spectral domain Optical Coherence Tomography. AO has the same use as in microscopy given that the eye also has changes in its refractive index which jeopardizes getting a clear image.

The core of this survey consists of three main background chapters that can be read independently and that provide the theoretical support to the results presented afterwards. In Chapter 2, a small introduction to AO is presented, where each phase is given individual in-depth treatment. In Chapter 3, the B-splines framework will be described. The B-splines will be useful to parametrize the wavefront locally. Besides that, the framework provides a set of linear constraints between that ensure smoothness of the global function up to a certain degree. In the last of the three core chapters, Chapter 4, a brief outline of some significant results in distributed optimization are presented.

Chapter 5 concerning the current results will provide the link that binds the previous three chapters together. In that chapter, the current implementation of a centralized and distributed algorithm for wavefront reconstruction is presented. The reconstruction is made by estimating the coefficients of the local splines basis functions from the intensity distribution created by a (Shack-)Hartmann sensor.

1-1 Nomenclature

The symbol $(\cdot)^*$ denotes the complex conjugate number of (\cdot) ; it can also be used to represent the optimal result from an optimization problem. The symbol $(\cdot)^T$ represents the transpose of (\cdot) .

Row or column vectors are represented using boldface lower-case symbols such as \mathbf{x} . Boldface and upper-case symbols, such as \mathbf{A} , are used for matrices. Regular font, x_1 , denotes a scalar variable. The hat symbol, $\hat{(\cdot)}$, is used to designate the estimate of (\cdot) .

The calligraphic notation, \mathcal{T} or \mathcal{N} , can represent sets or probability density functions. The tilde symbol, \sim , is used to denote the probability density function of a random variable. The operator $\langle \cdot \rangle$ denotes the expected value of a random variable.

Some matrices are characterized with the acronym (S)PD, which means that the matrix is (semi-)positive definite. A matrix \mathbf{M} which is symmetric and with dimensions $n \times n$, is said to be (semi-)positive definite if it follows that $\mathbf{z}^T \mathbf{M} \mathbf{z} (\geq) > 0$ for any non-zero vector \mathbf{z} .

In order to assess the complexity and execution time of the algorithms the big-O notation will be used. For instance, if an algorithm would have quadratic complexity with respect to a

variable b we would write $\mathcal{O}(b^2)$). This means that if the algorithm needs 100 floating-point operations (FLOPs) when $b = 1$, then for $b = 2$ the algorithm would require 400 FLOPs.

Adaptive Optics: an overview

High resolution imaging with telescopes, microscopes or lithography machines is often hampered by the presence of aberrations in the wavefront. Such aberrations are induced in various ways. For example, in astronomical observations with ground based telescopes, the aberrations are due to atmospheric turbulence, temperature gradients, etc. AO was proposed more than half a century ago [6], but is now more and more being used to correct these aberrations in real-time. An AO system consists of a sensor measuring information from which the wavefront aberrations can be reconstructed and an actuator to correct these aberrations. For classical real-time AO control where the bandwidth of the feedback controller is far below the first resonance frequency of the deformable mirror, used as an actuator, the key problem is the reconstruction of the wavefront, although research is being conducted in all the different stages of the AO loop.

cite Linnick as he independently proposed AO slightly after, 1957, than Babcock

In Section 2-1 the AO control problem is presented in an astronomical context. The chapter proceeds with Section 2-2, where the inner workings of the wavefront sensors are explained with a special emphasis in the Shack-Hartmann sensor. A comprehensive survey of classical and contemporary wavefront reconstruction methods is presented in Section 2-3. The last section of this chapter, Section 2-4, concerns the classical and the distributed control of the deformable mirror.

2-1 The Adaptive Optics Control Problem

To explain the principle of AO, and the role of wavefront reconstruction in the closed loop, we will briefly outline an AO application in an astronomical context. For that purpose, consider the schematic drawing in Figure 2-1. When light from a distant star arrives at the outer layers of the atmosphere, it has a flat plane wavefront. A wavefront is described by the following equation (in phasor notation),

$$\varphi(\mathbf{r}, t) = A(\mathbf{r}, t) \exp(\phi(\mathbf{r}, t)), \quad (2-1)$$

where $\mathbf{r} \in \mathbb{R}^2$ specifies the spatial position in the telescope aperture and t denotes time. A flat wavefront is such that its phase profile is $\phi(\mathbf{r}, t) = 0$ and, hence, if an image was captured from that wavefront it would not have any blurs in the intensity distribution $A(\mathbf{r}, t)$. However, this flat wavefront will reach the telescope deformed as the turbulent atmosphere will introduce time and space varying optical path length differences. This gives rise to a turbulence induced phase profile $\phi(\mathbf{r}, t)$. The AO system tries to cancel out these wavefront distortions by actively introducing optical path length differences of opposite sign.

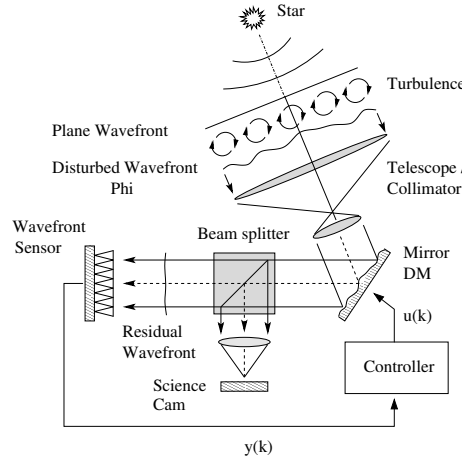


Figure 2-1: Schematic representation of an AO system, and its main components.

An AO system is typically composed of the following components – a wavefront sensor (WFS), a wavefront corrector element to influence the phase and a feedback controller. In most systems, like the one depicted in Figure 2-1, the wavefront corrector element is a deformable mirror (DM). For the ease of discussion we will simply assume that the active component is a DM.

Light that “enters” the AO system is first directed to the DM. By changing the mirror shape in real-time, the DM is able to apply a time-varying phase correction $\phi_{dm}(r, t)$. The residual phase error is the difference between the turbulence induced wavefront and the applied correction, i.e. $\epsilon = \phi - \phi_{dm}$. After applying the wavefront correction, a beam splitter divides the reflected light beam in two parts. The first part of the corrected light beam leaves the AO system and is used by the science camera for object image formation. The remaining light is directed to the WFS, which provides quantitative information about the residual wavefront. Based on the WFS measurements $s(\cdot)$, the controller has to determine the actuator inputs $u(\cdot)$ to the DM. The controller should adapt the input signal in such a way that the DM cancels out most of the distortions. The latter degree of compensation is specified in terms of control criteria, like the so-called \mathcal{H}_2 criterium [7].

By counteracting the wavefront distortions, AO is able to reduce the degrading effect of atmospheric turbulence on the imaging process. The goal of an AO system is to keep the wavefront of the light reaching the science camera to be as flat as possible. In this way, the corrected image can be recorded without being spread out when using long exposure times. By using AO, large ground-based based telescopes may reach close to diffraction limited performance in the near infrared [8, 9].

The next section will focus on one of the components of the AO system depicted in 2-1, the wavefront sensor.

2-2 Wavefront sensors

Similarly to our eyes, the current types of image sensors can't measure the wavefront directly, both magnitude and phase, but only the intensity of the light. The reason behind this is that the sensors are only sensitive to brightness levels.

When the imaging system and/or the transmission medium disturbs the spherical (or planar in case of a source at infinity) wavefront, blurring of the image occurs. To deblur the image one can estimate the phase of the wavefront so as to compensate for it in order to obtain a flat phased wavefront again.

We can divide imaging sensors in two main categories: pupil plane sensors and focal plane sensors. The ones relevant in the scope of this project are the pupil plane ones of which the Shack-Hartmann sensor will be described in Section 2-2-2. However, the principle that motivated the invention of such sensors is explained firstly in Section 2-2-1. The following sections follow the structure and nomenclature of [10].

2-2-1 Focal spot deviation

To exemplify this principle, let us consider a point source, such as a star, to continue the astronomical example started in Section 2-1.

The image of such a point source in an ideal ground-based telescope without the presence of atmosphere is shaped by the diffraction inherent to the diameter of the telescope and the wavelength of the light that is being captured. Looking at Figure 2-2 the first dark ring defines the resolution (according to Rayleigh's resolution criterion [source??](#)) and is given by $1,22\lambda/D$, where D represents the diameter and λ the wavelength of the incident wavefront.

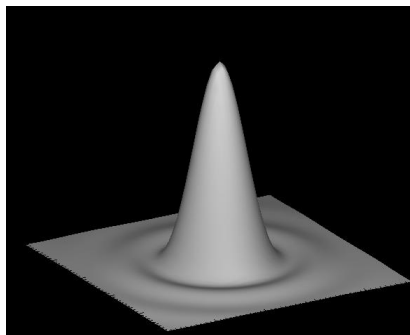


Figure 2-2: Airy Disk

From a control engineering perspective, the image of a point source under ideal condition can be considered as the 2-D impulse response of the system.

Let us now consider that an aberration distorts the perfect Airy disk. In the case where the aberration is only a tilt ([see Figure](#)), the effect on the deformed image can be computed

analytically. When the deviation due to tilting the wavefront is denoted by $\phi(x, y)$ it has been shown that the perturbed spot deviates from its center (with the ideal flat wavefront) by the distance Δx given by:

$$\Delta x = \kappa \frac{d\phi}{dx} \quad (2-2)$$

where κ is a constant parameter determined by the optical parameters such as pupil size, distance between pupil and lens, etc. The same formula holds for the deviation in the y direction, Δy .

SOME IMAGES GENERATED BY ME: they should contain a simple tilt and the way the diffraction pattern (and its centroid move). Besides that a more complicated wavefront should be represented and the resulting tilt that can be defined from the centroid which approximates the phase.

2-2-2 Shack-Hartmann sensor

In the previous section, we considered the whole wavefront phase distribution as being described by just a tilt. Normally, wavefront aberrations are more complex and so Hartmann, in the 1900, had the idea of constructing an array of apertures that would sample the wavefront (see Figure 2-3). The aberration "seen by" the aperture can then be approximated by a tilt. Thus, if we sample the wavefront with a finer aperture grid the approximation power is rendered higher as we can describe more complex wavefronts.

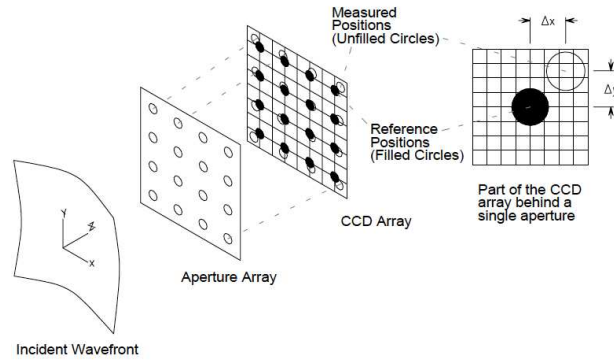


Figure 2-3: Schematic of an Hartmann array of pupils (or apertures). (source: "Hartmann Wavefront Analyzer Tutorial, Spiricon Laser Beam Diagnostics")

Roland Shack and Ben Platt [11] later proposed to replace the aperture array by a lenslet array. The idea stemmed from the fact that the Hartmann array was producing inaccurate and low intensity images which could be avoided by focusing the sampled rays with a set of lenses. This sensor is still used in numerous Adaptive Optics applications. The reader may refer to the introductory chapter for an overview of such applications.

In Figure 2-4 a simple 1 dimensional version of the principle behind the Shack-Hartmann sensor is shown. The array of lenses is parallel to a photon sensor, typically a Charge-Coupled Device (CCD) camera or a quad cell ¹. For each aperture (lens), the deviation of the

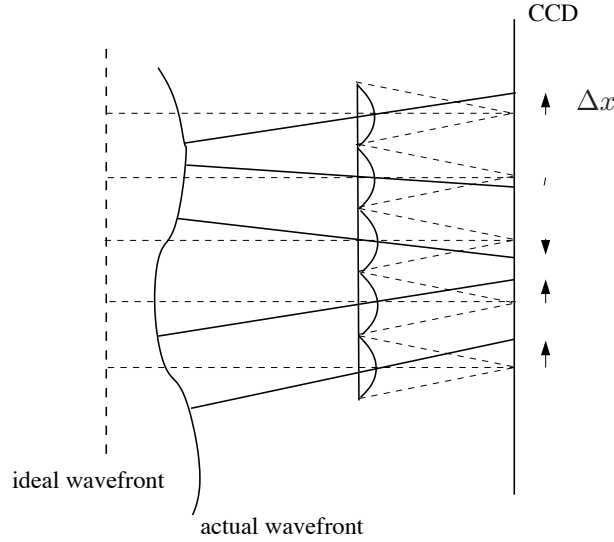


Figure 2-4: 1 dimensional representation of a Shack-Hartmann sensor. (source: Lecture notes on Control for High Resolution Imaging)

focal spot from the center location is given by Equation 2-2 and denoted in 2D by a deviation in x and y direction as:

$$\Delta x(i, j) = \kappa_x \frac{\partial \phi(x_i, y_j)}{\partial x} + \eta_x(i, j) \quad (2-3)$$

$$\Delta y(i, j) = \kappa_y \frac{\partial \phi(x_i, y_j)}{\partial y} + \eta_y(i, j) \quad (2-4)$$

where i, j represent the lenslet (aperture) in the i -th row, j -th column of the rectangular lenslet (aperture) array; x_i and y_i are the spatial coordinates of the wavefront and $\eta_x(i, j)$ and $\eta_y(i, j)$ represent the measurement noise and the effect from higher order aberrations that differ from just the tilt of the wavefront that can be estimated in the $(i\text{-th}, j\text{-th})$ aperture. The κ_x and κ_y are a purely geometric quantity. Roughly, $\kappa = z$ through a series of trigonometric approximations, where z is the distance that separates the array from the camera. The full derivation can be seen in the Appendix A-2.

Due to diffraction (as explained in 2-2-1) not a single pixel will in general be highlighted by the projection of a point source on the CCD camera, but an area. In order to compute the slopes, a centroid algorithm is applied [14], such that we can measure how much did the centroid changed from its ideal position (flat wavefront),

¹The CCD, concept which gave George Smith and Williard Boyle the Nobel Prize in Physics in 2009, converts the incoming photons into electron charges at a semiconductor-oxide interface; afterwards it is able to read out these charges by means of measuring the charge of the capacitor associated with each pixel [12]. The quad-cell bases its operating principles in a photodiode [13].

$$\begin{aligned}
s_x(i, j) &= \frac{1}{z} \frac{\sum_{u,v} u \Delta_x I(u, v)}{\sum_{u,v} I(u, v)} = \frac{\partial \phi(x_i, y_j)}{\partial x} + \tilde{\eta}_x(i, j), \\
s_y(i, j) &= \frac{1}{z} \frac{\sum_{u,v} v \Delta_y I(u, v)}{\sum_{u,v} I(u, v)} = \frac{\partial \phi(x_i, y_j)}{\partial y} + \tilde{\eta}_y(i, j).
\end{aligned} \tag{2-5}$$

$I(u, v)$ is the intensity measured in the pixel in the u -th row and v -th column of the CCD camera; Δx and Δy are the spacing of the pixels along the x and the y axis, respectively.

Although we presented the general formula of the centroid algorithm, the pairs (u, v) where the summation in Eq. (2-5) is performed were not specified. A straight-forward implementation is to take the maximum intensity value closest to where the maximum would ideally lie and select all the pixels around the maximum using a rectangular or circular window. Other methods include more involved thresholding mechanisms [15] or the inclusion of a weighting rectangular or Gaussian window [16]. Furthermore, there are also matched filter approaches such as the one presented in [17] and the references therein. In a [18] comparison between the different techniques is presented.

conclusions from the survey in [18]!!!

2-3 Wavefront reconstruction

The seminal works from Fried [19], Hudgin [20] and Southwell [1], among others, created the classical wavefront reconstruction algorithms which influenced most of the methods used nowadays. Fried and Hudgin developed a zonal reconstruction method which, despite its simplicity, has been optimized and improved in [21, 22, 23, 24].

Southwell presented a phase-retrieval method which was coined as modal reconstruction. This method was later enhanced in terms of computational complexity in [25, 26].

This section starts by presenting the classical reconstruction algorithms, zonal and modal. After those, the state-of-the-art methods are presented and an analysis regarding their computational complexity and their performance is made.

Coen says in the SABRE paper that Modal reconstruction methods using Zernike or KL polynomials lack approximation power. What?

Also refers that its implementation in non-circular grids is non-trivial. I will have to compare it with the one I've made and the one that Alessandro has made.

2-3-1 Zonal Reconstruction

Apparently Fried is defined with the exception of two constants while Hudgin needs only one. Can you give physical meaning to those rank deficiencies?

Present the case where we have a priori info that allows us to have a minimum variance estimator

Once the slope measurements are available (via, e.g., the centroid method in Eq. (2-5)), a linear model can be created such that it relates the unknown phase values with the slope of

the phase via a finite difference approach. Fried ([19]) and Hudgin ([20]) were the ones who firstly described this method, although each of them related the phase values and the slope measurements differently (see Figure 2-5).

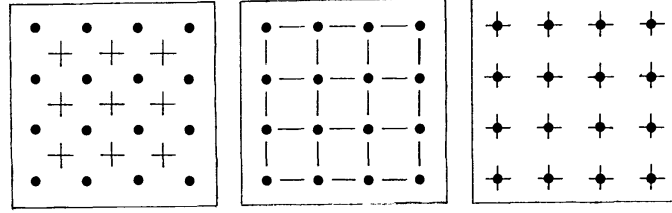


Figure 2-5: Phase points (denoted with a circle) and slopes (denoted with a dash) used by (Left and center) Hudgin and (Right) Fried (image retrieved from [1])

The equations that establish the relations in, e.g., Fried's finite difference model are

$$\begin{aligned} s_x(i, j) &= \frac{(\phi(i+1, j) + \phi(i+1, j+1))/2 - (\phi(i, j) + \phi(i, j+1))/2}{h}, \\ s_y(i, j) &= \frac{(\phi(i, j+1) + \phi(i+1, j+1))/2 - (\phi(i, j) + \phi(i+1, j))/2}{h}, \end{aligned} \quad (2-6)$$

where h represents, for a uniformly arranged lenslet (aperture) array, the distance between the center of the lenslet (aperture) in the pupil plane.

Given Eq. (2-6) and Figure 2-5, the derivation of the equations in Hudgin's finite difference model is straightforward.

We can then stack the slopes in a vector \mathbf{s} and the unknown phase values in another vector ϕ such that their linear relationship can be compactly represented as follows

$$\mathbf{s} = \mathbf{A}\phi, \quad (2-7)$$

where \mathbf{A} is the matrix that defines the finite differences, \mathbf{s} are the stacked slope measurements, and ϕ the stacked phase points.

Dimensions of the matrix and their ranks for Fried and Hudgin?

A standard solution for the problem of finding ϕ is to compute the pseudo-inverse matrix $\mathbf{A}^+ = (\mathbf{A}^T \mathbf{A})^{-1} \mathbf{A}^T$ thus yielding $\phi = \mathbf{A}^+ \mathbf{s}$.

However, due to the fact that any constant wavefront added to the obtained solution also satisfies the model, the problem is ill-posed which means that the matrix $\mathbf{A}^T \mathbf{A}$ is singular.

In [27], matrix \mathbf{A} is extended in such a way that $\mathbf{A}^T \mathbf{A}$ is fully ranked. This extension is made by adding another set of equations to the system such that the piston mode is fixed at 0.

2-3-2 Modal Reconstruction

This type of reconstruction is also formulated as a least-squares problem although the underlying principle is different. The seminal work was done by Southwell in [1] some years after Fried presented the zonal reconstruction method.

The first step is to parametrize the entire phase distribution $\phi(x, y)$ in terms of K arbitrary orthogonal and normalized basis functions F_k

$$\phi(x, y) = \sum_{k=0}^K a_k F_k(x, y), \quad (2-8)$$

where a_k are the coefficients to be determined.

Differentiating the phase expression in (2-8) the slope model is obtained

$$\begin{aligned} s_x(x, y) &= \sum_{k=1}^K a_k \frac{\partial F_k(x, y)}{\partial x}, \\ s_y(x, y) &= \sum_{k=1}^K a_k \frac{\partial F_k(x, y)}{\partial y}. \end{aligned} \quad (2-9)$$

The slope measurements in Eq. (2-9) are defined in a continuous domain by the (x, y) pair. However, implementation purposes the domain needs to be discretized for implementation purposes. We can, thus, sample the domain according to the capabilities of our wavefront sensor and replace the continuous pair (x, y) by a discrete one, (i, j) .

After defining a suitable set of basis functions (Legendre [1], Zernike [28] or complex exponentials [25]) Eq. (2-9) can be reformulated in matrix form

$$\mathbf{s} = \mathbf{A} \mathbf{a} \quad (2-10)$$

At this point one may wonder about the absence of the a_0 coefficient in the slope model. This coefficient can not be determined as it represents the piston mode. However, if you use basis functions that have zero-mean (as it is done in [1]) then the estimated phase will also be zero-mean if the piston mode is set to 0 ($a_0 = 0$). Due to this absence, we guarantee that the normal equations are not ill conditioned.

2-3-3 Novel methods for wavefront reconstruction

After the breakthrough in wavefront reconstruction in the late 70s and early 80s, the technological developments that led to the construction of larger optics measurement and actuation devices have driven researchers to look for faster reconstruction techniques, implementable in real-time environments.

Fast Fourier Transform

The work of Poyneer et al. in [26] uses the Fast-Fourier Transform (FFT) to reconstruct the wavefront improving the earlier works from by Freischlad [25]. The algorithm Freischlad developed can be explained in the light of modal reconstruction algorithms. However, the basis functions are defined as complex exponentials in such way that the wavefront can be described as a Discrete Fourier Transform (DFT) of the basis functions weighting coefficients.

After some manipulation, those coefficients can be estimated by taking the DFT of the slope measurements together with other scaling factors. Poyneer develops this idea and applies it to circular sensor configurations and other grid geometries.

Multigrid methods

Gilles [29] formulates the reconstruction in a least-squares sense using a multigrid phase retrieval method to perform a zonal reconstruction. However, it restricts the problem formulation for astronomical applications only. Therefore it can enhance the quality of the estimate in terms of its variance if the characteristics of the atmospheric phase covariance matrix ($\mathbf{C}_{\phi\phi} = \langle \phi\phi^T \rangle$) and the noise affecting the slope measurements ($\mathbf{C}_{\eta\eta} = \langle \eta\eta^T \rangle$) are known. In this paper, it is assumed that $\mathbf{C}_{\eta\eta} = \sigma^2 \mathbf{I}$. As for the atmospheric turbulence, it is proved that $\mathbf{C}_{\phi\phi}$ can be closely approximated by a Semi-Positive Definite (SPD) matrix, $\tilde{\mathbf{C}}_{\phi\phi}$. By minimizing $\langle \|\mathbf{R}\mathbf{s} - \phi\|_2^2 \rangle$, where \mathbf{R} is the reconstructor matrix, we obtain

$$\mathbf{B}\phi = \mathbf{G}^T \mathbf{s}, \quad \mathbf{B} = \mathbf{G}^T \mathbf{G} + \sigma^2 \tilde{\mathbf{C}}_{\phi\phi}^{-1}. \quad (2-11)$$

Due to the fact that $\tilde{\mathbf{C}}_{\phi\phi}$ is SPD, its inverse will also have that property. Hence, matrix \mathbf{B} will also be SPD because it is the sum of two SPD matrices given that $\mathbf{G}^T \mathbf{G}$ is symmetric SPD and sparse.

Equation (2-11) can then be solved iteratively using the Gauss-Seidel (GS) iterations [30]. However this procedure is not very effective in eliminating the low frequency-error. For this reason, the GS method is called a smoother. Different smoothers can be devised to be more effective at lower or higher frequencies. After a solution is obtained with the classical GS, the residual is projected onto a coarser phase grid and a smoother more prone to correct lower frequency errors is applied. This can be done recursively until we achieve the coarsest resolution we defined. The method, when applied recursively is called multigrid.

Vogel [31] refines the work by Gilles by generalizing to other sensor-actuator geometries.

Wavelet-based methods

In [32] a reconstruction method using wavelets is presented which also has linear complexity ($13N$, where N represents the number of unknown phase points). This method is highly scalable and uses a modified 2-D Haar wavelet filterbank which processes the wavefront gradients directly.

Fractal Iterative Method

In [22], Thiébaud and Tallon present an iterative method called FRiM (Fractal Iterative Method) with linear complexity ($\mathcal{O}(N)$, where N represents the number of actuators). They make use of the fractal (self-similarity) of the Kolmogorov phase screens [33] and are able to avoid inverting the covariance matrix of a turbulence screen.

Cumulative reconstructor

Another method was proposed by [23] and [24] called CuRe (Cumulative Reconstructor) where a very low computational effort ($\mathcal{O}(N)$) was achieved and the results were comparable in terms of accuracy with the standard zonal reconstruction methods. This algorithm works by integrating cumulative the horizontal and the vertical lines of the phase point grid. Using a grid from Hudgins (Figure 2-5, center) the phase profile can be created by joining two adjacent points in a given direction by drawing a line whose steepness will be given by the slope measurements. After doing this (parallelizable) procedure for both horizontal and vertical lines an average horizontal and vertical profile is computed and the lines are shifted according to this profile.

Spline-based methods

There is one recent method which parametrizes the wavefront using splines which is one of the seminal works that gave rise to this graduation project. The algorithm is called SABRE and was presented by de Visser in [34]. It parametrizes locally the wavefront using splines defined in non-overlapping triangular regions. It claims to have a bigger approximation power than the common modal modes due to the partitioning of the wavefront. Although it is MVM method it has a very high potential for parallelization and is suitable to be used in for any kind of sensor-actuator arrangement. The results were comparable to the classical zonal reconstruction methods using a square uniform phase point grid. A distributed version of this algorithm can be found in [35].

[Point to a more in-depth analysis of the SABRE and D-SABRE methods](#)

Non-linear intensity phase retrieval

Another novel method for WFR is the one presented by Polo in [5]. In this paper, a phase-retrieval method is proposed for EUVL applications using the Hartmann wavefront sensor as the SH sensor blocks the wavelengths used in EUVL technology. The main difference in this method is that the centroid algorithm is not used. The wavefront reconstruction is performed using directly the intensity distribution.

In order to retrieve the phase information, a non-linear model is created that relates the unknown wavefront at the pupil plane and the intensity distribution at the propagation plane². A non-linear least squares algorithm is employed afterwards in order to minimize the discrepancies between the experimental and the modelled intensity distribution. The minimization is made with respect to the coefficients of the Zernike basis functions that parametrize the unknown wavefront.

[TABLE with all the algorithms and their complexity and some observations](#)

When dealing with static aberrations, these wavefront reconstruction methods are enough to compensate them by inputting the necessary corrections to a deformable mirror. However, if

²The fact that we are using, in the context of [5], a Hartmann sensor, which has no lenses, is why the intensity distribution is said to be in the *propagation* plane. If we were referring to the same plane for the SH sensor the term *focal* plane would be the most appropriate.

the aberrations change in time, then an active control mechanism is required. This topic is discussed in the next section.

2-4 Closed loop control with Deformable Mirror

The active element in an AO setup is the deformable mirror. When actuated, the DM is able to effectively minimize the effects of phase aberrations in real-time. In Section 2-4-1, a classical control approach is presented and in the next section, Section 2-4-2, we refer to some references on distributed control methods.

2-4-1 Classical approach

The classical approach for controlling a deformable mirror in an AO setup can be seen in the block diagram of 2-6.

The process begins when the incident phase of the wavefront $\phi(k)$ at time instant k is reflected by the mirror. The DM modifies the incident phase as it introduces a phase change of $-\phi_m(k)$. The resulting reflected wavefront is given by $\epsilon_\phi(k) = \phi(k) - \phi_m(k)$ which enters the WFS and is corrupted by noise denoted by $\eta(k)$. This WFS measurement is denoted as $\epsilon_y(k)$. The WFS block has some dynamics which are not explicit in the block diagram: it needs to integrate the photons as they arrive and should contain a delay as to model the communication overhead and the processing time.

The corrupted measurement is then used to reconstruct the wavefront. In this block diagram the reconstruction is depicted as a linear operation by means of the reconstruction matrix \mathbf{R} . Although the great majority of the algorithms described in this survey are linear, that need not be so as a non-linear algorithm such as the one in [5] may be used in the reconstruction. Regardless of what method is employed, the reconstructed wavefront is given by $\hat{\epsilon}_\phi$.

After the reconstruction, matrix \mathbf{F} is responsible for projecting the reconstructed wavefront into the actuator space. The construction of matrix \mathbf{F} requires knowledge of the model of the DM as it provides an inverse mapping between a desired phase and the actuator commands. The actuator commands generated by matrix \mathbf{F} are then filtered by the controller and can be provided to the deformable mirror.

If we do not have access to an experimental setup and want to test an algorithm, the loop could be closed by having the actuator commands transformed into the phase modification that the mirror will provide. For that we need a model of the mirror (usually a linear model, represented by a matrix \mathbf{H}). With that final link the full feedback loop is completed.

The objective of this loop is to minimize the variance of the estimate over the actuator space,

$$\text{minimize } \text{var}(\hat{\epsilon}_\phi). \quad (2-12)$$

This is achieved by using an integral controller that has an incremental effect. If we denote the actuator commands by $u(k)$, the filtering made by the integral controller can be written as,

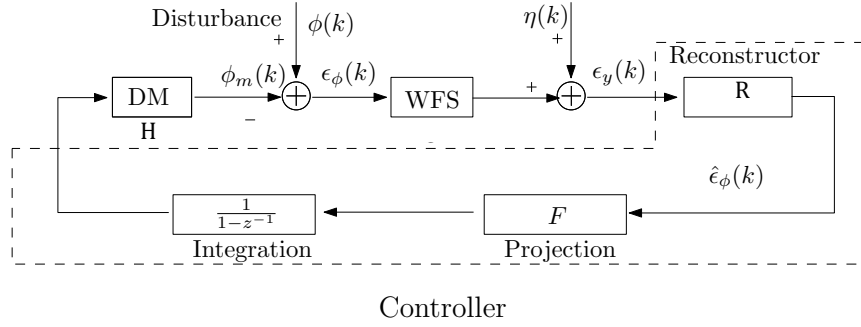


Figure 2-6: Block diagram of a classical feedback loop used in Adaptive Optics

$$u(k+1) = u(k) + \mu \Delta u(k+1), \quad (2-13)$$

where μ denotes the integral gain. This stems from the fact that we are only measuring the residual wavefront in the WFS and hence only an incremental input needs to be applied.

2-4-2 Distributed approach

The need for a distributed control approach in AO is justified by the fact that the next generation of large-scale ground-based telescopes will involve a very high number of actuators and sensors. Besides that, the reconstruction of the wavefront and the computation of the control signal should be done in less than 1ms [36]. Therefore, the need for distributed algorithms for reconstruction and control are required.

Massioni in [37], [38] uses a decomposition approach to the complete DM model where he assumes that each of its actuators is an identical subsystem. The structure of the decomposed system is given by a "pattern matrix" which is sparse due to the fact that each subsystem only influences its nearest neighbours. It is possible to take advantage of the sparsity of the "pattern matrix" and devise an \mathcal{H}_2 optimal controller that is scalable with respect to the number of actuators.

It is said that the subsystems are identical. However, the boundary conditions may create some problems! How does Massioni deal with that?

Chapter 3

B-Splines framework

The nomenclature used in this chapter will follow closely the one presented in [34, 39]. For a more in-depth treatment of the multivariate simplex B-Splines the reader is advised to read [40] or the seminal work [41].

A spline is a potentially multivariate, piecewise function which is described by a polynomial. It has a certain degree of continuity between its individual segments. The usefulness of this piecewise nature is that it can be used to fit data that is too complex to be approximated with a single functional piece.

Among the several types of existent splines, this work will focus in 2 dimensional simplex splines given their usefulness to model, e.g. the phase distributions in a wavefront or the profile of a deformable mirror. These splines were chosen mainly due to their inherent suitability to be incorporated in distributed algorithms.

The simplex splines can be defined in several geometric structures called simplices. A simplex is a polyhedral formed by the convex hull of $n + 1$ points if the spline is defined in \mathbb{R}^n . In the two dimensional case relevant to this work, the simplices are triangles which can be defined using three non-degenerate vertices $\mathbf{v}_0, \mathbf{v}_1, \mathbf{v}_2 \in \mathbb{R}^2$.

The basis polynomials of the simplex B-Splines are defined in local barycentric coordinates defined only inside a particular simplex. The reason for this barycentric representation is that it is easier to evaluate the function when working in this local basis. Given a certain point $\mathbf{x} = (x, y) \in \mathbb{R}^2$ belonging to the Cartesian plane a barycentric coordinate in \mathbb{R}^3 can be determined as follows:

$$\begin{bmatrix} b_1 \\ b_2 \end{bmatrix} = \mathbf{V}^{-1} \begin{bmatrix} x \\ y \end{bmatrix} \quad (3-1)$$

$$b_0 = 1 - b_1 - b_2 \quad (3-2)$$

where the transformation matrix \mathbf{V} is defined as

$$\mathbf{V} = \begin{bmatrix} \mathbf{v}_1 - \mathbf{v}_0 & \mathbf{v}_2 - \mathbf{v}_0 \end{bmatrix} \quad (3-3)$$

To simplify the notation, the transformation from Cartesian to Barycentric coordinates from $\mathbf{x} \in \mathbb{R}^2$ to $\mathbf{b} \in \mathbb{R}^3$ will be denoted as:

$$\mathbf{b}(\mathbf{x}) = (b_0, b_1, b_2) \quad (3-4)$$

A distinguishing feature of any spline is its locality. This property can be used in order to achieve a higher approximation power, as we can combine several simplices and devise a partition of the domain which forms a triangulation. This triangulation is usually represented by \mathcal{T} and consists of non-overlapping simplices.

how to come up with the triangulation from a set of knots? describe it without being too general and not too specific

Now that the barycentric coordinates and the simplices have been clearly defined, we can introduce the splines basis functions. Using the fact that any polynomial of total degree d can be expanded into a sum of monomials we can write the following expression in the barycentric coordinate system

$$(b_0 + b_1 + b_2)^d = \sum_{\kappa_0 + \kappa_1 + \kappa_2 = d} \frac{d!}{\kappa_0! \kappa_1! \kappa_2!} b_0^{\kappa_0} b_1^{\kappa_1} b_2^{\kappa_2} \quad (3-5)$$

where

$$|\kappa| = \kappa_0 + \kappa_1 + \kappa_2 = d, \quad \kappa_0, \kappa_1, \kappa_2 \geq 0 \quad (3-6)$$

Each individual basis function is defined as one of the monomials in (3-5). This function takes non-zero values only inside a certain simplex t and can be written as follows

$$B_{\kappa}^d(\mathbf{b}(\mathbf{x})) = \begin{cases} \frac{d!}{\kappa_0! \kappa_1! \kappa_2!} b_0^{\kappa_0} b_1^{\kappa_1} b_2^{\kappa_2} & , \mathbf{x} \in t \\ 0 & , \mathbf{x} \notin t \end{cases} \quad (3-7)$$

The total number of these basis functions for a certain spline degree d is

$$\hat{d} = \frac{(d+2)!}{2d!} \quad (3-8)$$

Weighting the \hat{d} basis functions with their corresponding coefficient c^t yields a B-form polynomial $p(b(\mathbf{x}))$

$$p(b(\mathbf{x})) = \begin{cases} \sum_{|\kappa|=d} c_{\kappa}^t B_{\kappa}^d(b(\mathbf{x})) & , \mathbf{x} \in t \\ 0 & , \mathbf{x} \notin t \end{cases} \quad (3-9)$$

Equation (3-9) can easily be translated into vector form firstly by putting each of the basis functions evaluated at a certain point \mathbf{x} in the rows of the vector $\mathbf{B}^d(\mathbf{b}(\mathbf{x}))$ and secondly by placing the weighting coefficients of the basis functions in a column vector \mathbf{c}^t , sorted accordingly.

$$p(\mathbf{b}(\mathbf{x})) = \begin{cases} \mathbf{B}^d(\mathbf{b}(\mathbf{x}))\mathbf{c}^t & , \mathbf{x} \in t \\ 0 & , \mathbf{x} \notin t \end{cases} \quad (3-10)$$

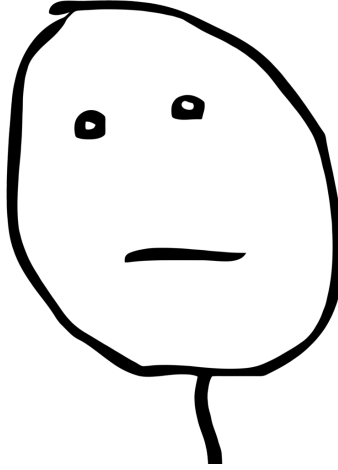


Figure 3-1: IMAGE OF A B-NET

It is crucial to bear in mind, however, that the vector \mathbf{x} is only defined in one single triangle t . If the process is repeated for the J triangles pertaining to the triangulation \mathcal{T} we will have the following function s_d

$$s_d(\mathbf{b}(\mathbf{x})) = \mathbf{B}^d \mathbf{c} \quad (3-11)$$

To clarify the way Eq. (3-11) was constructed let us consider first the global vector \mathbf{B}^d which groups the information pertaining to all the simplices

$$\mathbf{B}^d = \begin{bmatrix} \mathbf{B}_{t_1}^d(\mathbf{b}(\mathbf{x})) & \mathbf{B}_{t_2}^d(\mathbf{b}(\mathbf{x})) & \cdots & \mathbf{B}_{t_J}^d(\mathbf{b}(\mathbf{x})) \end{bmatrix} \in \mathbb{R}^{1 \times Jd} \quad (3-12)$$

One must note, however, that when \mathbf{x} is defined outside the simplex t_j we will have $\mathbf{B}_{t_j}^d(\mathbf{b}(\mathbf{x})) = 0$ and, thus, the global \mathbf{B}^d will be sparse.

The global vector \mathbf{c} of B-coefficients in Eq. (3-11) follows the same construction guidelines of \mathbf{B}^d

$$\mathbf{c} = \begin{bmatrix} \mathbf{c}_{t_1}^T & \mathbf{c}_{t_1}^T & \dots & \mathbf{c}_{t_1}^T \end{bmatrix}^T \in \mathbb{R}^{J\hat{d} \times 1} \quad (3-13)$$

One of the main advantages of using B-splines is the fact one can force continuity of order r such that all m -th order derivatives, with $0 \leq m \leq r$, of two B-form polynomials defined on two neighbouring simplices are equal on the edge between the simplices. For C^r continuity there are a total of Q continuity conditions per simplex edge. Given that there are E edges, the total number of continuity conditions will be $Q \times E$.

$$Q = \sum_{m=0}^r (d - m + 1) \quad (3-14)$$

In [39], a general method was created to guarantee continuity between all the common edges of neighbouring B-form polynomials. The method yields a smoothness matrix \mathbf{H} that establishes a relationship between the coefficients of the neighbouring polynomials:

$$\mathbf{H}\mathbf{c} = 0 \quad (3-15)$$

This global smoothness matrix $\mathbf{H} \in \mathbb{R}^{QE \times J\hat{d}}$ in (3-15) has in each of its rows a single continuity condition. The vector \mathbf{c} is the one containing all the coefficients as presented in Eq. (3-11).

Distributed Optimization

This chapter focuses on distributed optimization, specially in an optimization method called alternate direction method of multipliers (ADMM). Before presenting ADMM, however, the precursors of this method must be discussed. We will start by explaining primal decomposition in Section 4-1. Afterwards, we will present the dual ascent and dual decomposition methods in Section 4-2 and 4-2-1, respectively. Then the method of multipliers in Section 4-2-2 will be discussed before finally presenting ADMM in Section 4-3.

4-1 Primal Decomposition

A very simple problem can be used to illustrate clearly the principle behind this decomposition method. Let us have the following unconstrained optimization problem

$$\text{minimize } f(\mathbf{x}) = f_1(\mathbf{x}_1, \mathbf{y}) + f_2(\mathbf{x}_2, \mathbf{y}), \quad (4-1)$$

where \mathbf{x}_1 and \mathbf{x}_2 are the "private" variables of functions f_1 and f_2 , respectively, and \mathbf{y} is the complicating variable that binds both the sub-problems together. If \mathbf{y} was not present the problem could be solved by minimizing f_1 and f_2 separately with respect to their private variables. If \mathbf{y} is present, we perform the following minimization

$$\begin{aligned} \phi_1(\mathbf{y}) &= \underset{\mathbf{x}_1}{\text{minimize}} f_1(\mathbf{x}_1, \mathbf{y}), \\ \phi_2(\mathbf{y}) &= \underset{\mathbf{x}_2}{\text{minimize}} f_2(\mathbf{x}_2, \mathbf{y}), \end{aligned} \quad (4-2)$$

followed by

$$\underset{\mathbf{y}}{\text{minimize}} \phi_1(\mathbf{y}) + \phi_2(\mathbf{y}). \quad (4-3)$$

This last minimization problem is called the *master problem*. Notice that, if the original problem is convex, the master problem is also convex. (in Boyd's lectures there's sth about this!).

A subgradient method can then be used to solve alternately the problems in Eq. (4-2) and the master problem in Eq. (4-3).

This decomposition method can also integrate constraints of the form $h(\mathbf{x}_1) + h(\mathbf{x}_2) \preceq 0$. The problem needs to be reformulated and an extra variable per each constraint must be added. Finally, the subgradient method can also be used to solve such a problem.

4-2 Dual Ascent

Let us consider the following canonical optimization problem with equality constraints

$$\begin{aligned} & \text{minimize } f(\mathbf{x}) \\ & \text{subject to } \mathbf{Ax} = \mathbf{b} \end{aligned} \quad (4-4)$$

where $\mathbf{x} \in \mathbb{R}^n$, $\mathbf{A} \in \mathbb{R}^{m \times n}$ and $f : \mathbb{R}^n \rightarrow \mathbb{R}$. This problem formulation will be denominated the primal problem as opposed to the dual problem which will be exposed next.

The Lagrangian for the problem in Eq. (4-4) is

$$\mathcal{L}(\mathbf{x}, \mathbf{y}) = f(\mathbf{x}) + \mathbf{y}^T(\mathbf{Ax} - \mathbf{b}) \quad (4-5)$$

and the dual function is

$$g(\mathbf{y}) = \inf_{\mathbf{x}} \mathcal{L}(\mathbf{x}, \mathbf{y}) \quad (4-6)$$

The maximization of g in Eq. (4-6) is called the dual problem. When strong duality ([42, Lecture 8]) holds, the optimal values for both the primal and dual problems are equal and one can extract the optimal point \mathbf{x}^* from an optimal point \mathbf{y}^* as follows

$$\mathbf{x}^* = \arg \min_{\mathbf{x}} \mathcal{L}(\mathbf{x}, \mathbf{y}^*) \quad (4-7)$$

provided that there is only one minimizer \mathbf{y}^* .

With the dual ascent method the dual problem is solved by using the gradient ascent which translates into the following procedure

$$\mathbf{x}^{k+1} = \arg \min_{\mathbf{x}} \mathcal{L}(\mathbf{x}, \mathbf{y}^k) \quad (4-8)$$

$$\mathbf{y}^{k+1} = \mathbf{y}^k + \alpha^k (\mathbf{Ax}^{k+1} - \mathbf{b}), \quad (4-9)$$

Notice that $\mathbf{A}\mathbf{x}^{k+1} - \mathbf{b}$ is the gradient of \mathcal{L} with respect to \mathbf{y} . In the update of the dual variable, we must follow the direction of the positive gradient and thus maximizing the dual variable value. Hence, the name of the method - dual ascent.

The advantage of the dual ascent method will become clearer as it enable us to introduce dual decomposition.

4-2-1 Dual Decomposition

Besides primal decomposition, we can also decompose some separable optimization problems by expanding the objective functions into their Lagrangians and use a subgradient method to optimize both the primal variable and the dual variable. This method is called *dual decomposition* and the seminal idea was presented by Dantzig and Wolfe [43] and was applied to linear programming problems. Everett [44] presented a more general decomposition approach using the Lagrange multipliers, afterwards.

Let us assume that the problem setting is the same as in Eq. (4-4) objective function is separable, which means that we can write f as

$$f(\mathbf{x}) = \sum_{i=1}^N f_i(\mathbf{x}_i), \quad (4-10)$$

where $\mathbf{x} \in \mathbb{R}^n$ can be segmented into several subvectors $\mathbf{x}_i \in \mathbb{R}^{n_i}$ (with no components in common). If splitting f is possible then the partitioning of \mathbf{A} can be done swiftly in conformity with the partitioning of \mathbf{x} , such that $\mathbf{A}\mathbf{x} = \sum_{i=1}^N \mathbf{A}_i\mathbf{x}_i$.

The partitioning of both \mathbf{x} and \mathbf{A} make it possible to define the Lagrangian \mathcal{L} as follows

$$\mathcal{L}(\mathbf{x}, \mathbf{y}) = \sum_{i=1}^N f_i(\mathbf{x}_i) + \mathbf{y}\mathbf{A}_i\mathbf{x}_i - (1/N)\mathbf{y}\mathbf{b}, \quad (4-11)$$

which is also separable in \mathbf{x} . This separability means that Eq. (4-8) can be solved independently for each \mathbf{x}_i .

$$\mathbf{x}_i^{k+1} = \arg \min_{\mathbf{x}_i} \mathcal{L}_i(\mathbf{x}_i, \mathbf{y}^k), \quad (4-12)$$

$$\mathbf{y}^{k+1} = \mathbf{y}^k + \alpha^k (\mathbf{A}\mathbf{x}^{k+1} - \mathbf{b})., \quad (4-13)$$

After each \mathbf{x}_i is calculated the results are concatenated to form again \mathbf{x} and the dual variable \mathbf{y} can then be updated. The 2-steps in each iteration are thus called *gather* and *broadcast*. The residual $\mathbf{A}\mathbf{x}^{k+1} - \mathbf{b}$ is gathered from each individual processing unit and after the dual update the dual variable is broadcasted back.

4-2-2 Method of Multipliers

The method of multipliers appears as an extension of the dual ascent that can provide a more robust performance. This method uses the augmented Lagrangian ([45] and [46]) $\mathcal{L}_\rho = \mathcal{L} + (\rho/2)\|\mathbf{Ax} - \mathbf{b}\|_2^2$ which can be integrated in a problem formulation equivalent to the one in (4-4).

$$\begin{aligned} \min. \quad & f(\mathbf{x}) + (\rho/2)\|\mathbf{Ax} - \mathbf{b}\|_2^2, \\ \text{subject to} \quad & \mathbf{Ax} = \mathbf{b}. \end{aligned} \tag{4-14}$$

Notice that, for a feasible \mathbf{x} the extra term does not affect the objective function as the residual would be zero. We can solve this problem by applying the dual ascent method, which yields the following update expressions

$$\mathbf{x}^{k+1} = \arg \min_{\mathbf{x}} \mathcal{L}_\rho(\mathbf{x}, \mathbf{y}^k), \tag{4-15}$$

$$\mathbf{y}^{k+1} = \mathbf{y}^k + \rho^k(\mathbf{Ax}^{k+1} - \mathbf{b}). \tag{4-16}$$

However, this new augmented Lagrangian is no longer separable which jeopardizes the application of a such a method in a distributed optimization context.

4-3 ADMM

The alternate direction method of multipliers (ADMM) method enables us to join the decomposability of the dual ascent with the superior convergence properties of the method of multipliers. This method was firstly proposed by Glowinski and Marocco [47, Eqs. 9.7-9.9]¹ for a very specific finite-element approach to solve the non-linear Dirichlet problem. Gabay and Mercier's [48] problem formulation is more similar to the one presented in this section as they try to minimize expressions of the form $f(Av) + g(v)$, where A is a linear operator.

The canonical form of the problems that can be solved by ADMM is,

$$\begin{aligned} \text{minimize} \quad & f(\mathbf{x}) + g(\mathbf{z}), \\ \text{subject to} \quad & \mathbf{Ax} + \mathbf{Bz} = \mathbf{c}. \end{aligned} \tag{4-17}$$

This is a generalization of the work in [48] as the variables x and z do not need to be related by a linear operator.

If we were to apply the method of multipliers to solve the problem in Eq. (4-17) the two-step procedure would be described as follows,

$$\begin{aligned} (\mathbf{x}^{k+1}, \mathbf{z}^{k+1}) &= \arg \min_{\mathbf{x}, \mathbf{z}} \mathcal{L}_\rho(\mathbf{x}, \mathbf{z}, \mathbf{y}^k), \\ \mathbf{y}^{k+1} &= \mathbf{y}^k + \rho(\mathbf{Ax}^{k+1} + \mathbf{Bz}^{k+1} - \mathbf{c}). \end{aligned} \tag{4-18}$$

¹A less comprehensive English version of [47] can be found in [49].

In Eq. (4-18) the minimization is performed jointly in both \mathbf{x} and \mathbf{z} . In ADMM however, it is proposed that the variable update alternates between the two variables,

$$\begin{aligned}\mathbf{x}^{k+1} &= \arg \min_{\mathbf{x}} \mathcal{L}_{\rho}(\mathbf{x}, \mathbf{z}^k, \mathbf{y}^k), \\ \mathbf{z}^{k+1} &= \arg \min_{\mathbf{z}} \mathcal{L}_{\rho}(\mathbf{x}^{k+1}, \mathbf{z}, \mathbf{y}^k) \\ \mathbf{y}^{k+1} &= \mathbf{y}^k + \rho(\mathbf{A}\mathbf{x}^{k+1} + \mathbf{B}\mathbf{z}^{k+1} - \mathbf{c}).\end{aligned}\tag{4-19}$$

ADMM decomposes the method of multipliers by using Gauss-Seidel iterations (see [50, Section 10.1]) instead of a joint minimization.

The convergence properties and proofs are presented in [51, Section 3.2 and Appendix A].

4-3-1 Exchange problem

The exchange problem [51, Section 7.3.2] is a special case of the sharing problem [51, Section 7.3]. In the context of distributed wavefront reconstruction, the exchange problem will describe accurately the relationships between the subsystems and involved as will become clearer in Chapter 5.

Assuming that the objective function $f(\mathbf{x})$ is separable in N functions $f_i(x_i)$, each of them using only a part of vector \mathbf{x} , we can formulate the problem as follows,

$$\text{minimize} \quad \sum_{i=1}^N f_i(x_i) \tag{4-20}$$

$$\text{subject to} \quad \sum_{i=1}^N x_i = 0 \tag{4-21}$$

The solution to this problem is given by

$$x_i^{k+1} = \arg \min_{x_i} \left(f_i(x_i) + y^{kT} x_i + (\rho/2) \|x_i - (x_i^k - \bar{x}^k)\|_2^2 \right) \tag{4-22}$$

$$y^{k+1} = y^k + \rho \bar{x}^{k+1} \tag{4-23}$$

This means that in each iteration one must minimize the augmented Lagrangian for each of the x_i , $\forall i = 1, \dots, N$, and then update the duals.

Note that, in the canonical problem, all variables are connected with one another through the constraint $\sum_{i=1}^N x_i = 0$. This constraint can be generalized to one of the form $\mathbf{A}\mathbf{x} = \mathbf{b}$. Moreover the variable x_i is scalar and can also be generalized to a vector, \mathbf{x}_i . A specific realization of this generalization can be found in the last chapter, Chapter 5.

Chapter 5

Results

In this chapter, we present the preliminary results achieved regarding the creation and characterization of a distributed wavefront reconstruction algorithm. Firstly, we present a centralized algorithm which combines two novel principles in so far as it estimates the wavefront using B-Splines and uses the entire intensity measurements instead of the slope approximations. Secondly, an upgraded version of this algorithm which uses a Jacobian analysis to compress the amount of intensity measurements used is presented.

Present remaining sections...

Noise and Raffard derivations...

5-1 Intensity-based reconstruction using B-Splines

The Hartmann (resp. Shack-Hartmann) wavefront sensor consists of an array of apertures (resp. lenslets)¹ that sample the incoming wavefront. A centroiding algorithm (Sec. 2-2-2) then provides an *approximation* of the spatial slope of the wavefront for each aperture. This algorithm computes the center of mass of the intensity measurements collected by a detector (e.g. CCD camera) thus losing some of the information present in the intensity patterns. This will in general cause a loss in accuracy of the wavefront reconstruction results.

In order to preserve the main advantage of the centroid based wavefront reconstruction, that is, the *linearity* of the wavefront reconstruction problem, but to make direct use of the measured intensities as in [5] without first approximating the spatial slopes, a new wavefront reconstruction method is presented in this section. The method is based on the integration of two principles. The first is a physical principle where we perform a linearisation of the relationship between the local wavefront aberrations and the intensity measurements of the aperture that “sees” this local wavefront. The second is a numerical principle on the use

¹Given the applicability of this method both to the Hartmann and the Shack-Hartmann wavefront sensors, we will designate them both by referring to them abstractly as wavefront sensors, for the sake of brevity and simplicity. Both the lenslets and the apertures will be designated as apertures, also for the sake of brevity.

of B-splines to parametrize and reconstruct the unknown wavefront. The methodology of parametrizing the wavefront in the B-spline wavefront is based on the recent work in [39, 34].

The description of the new method is organized as follows: the main principles that support the method are described in Section 5-1-1. A simulation study of the new wavefront reconstruction method is presented in Section 5-1-2. There, a comparison is made with the classical modal reconstruction method [28] which uses slope measurements provided by the centroid algorithm [52]. The comparison is made in an open-loop and closed-loop configuration. For the classical AO feedback control it will be assumed that the deformable mirror is perfect and that the wavefront aberration is static. Such a classical AO control methodology described in a control engineering framework is e.g. given in [53, 7]. Finally we end this section with some concluding remarks.

5-1-1 Wavefront Reconstruction

The classical approaches mentioned in Sections 2-3-1 and 2-3-2 use the recorded intensities behind each aperture to extract an approximation of the local spatial gradient of the wavefront. In this section, we propose that all the recorded intensity measurements are used in the wavefront reconstruction. In the following subsection, we derive the model that relates the wavefront and the intensity measurements as well as the local linearisation of that model. Furthermore, we parametrize the wavefront using B-splines and define the phase-retrieval problem as a least-squares problem subject to linear constraints.

General intensity-based phase retrieval algorithm

In order to obtain a relation that relates the phase distribution of the wavefront and the intensity distribution measured by the wavefront sensor, we must define some quantities. Let the complex field $U(x, y, z)$ define the wavefront at a certain distance from the sampling sensor array. The complex field of the wavefront immediately after being transmitted ($z = 0$) by the sampling array can be described by its amplitude $A(x, y)$ and its unknown phase distribution $\Phi(x, y)$. Considering that the sampling array and the detection plane are separated by a distance L , we can define the complex field at $z = L$ by $U(x, y, L)$. The expressions that describe these two quantities are

Incoming Wavefront

$$U(x, y, 0) = A(x, y) \exp(i\nu\Phi(x, y)), \quad (5-1)$$

where ν represents the wavenumber.

Wavefront after propagation (Hartmann sensor)

$$U(x, y, L) = \mathcal{F}^{-1} [\mathcal{F}[U(x, y, 0)]H(f_x, f_y)], \quad (5-2)$$

where $H(f_x, f_y)$ represents the Rayleigh-Sommerfield transfer function [54] f_x and f_y are the spatial frequencies in the x and y directions, respectively

Wavefront at the focal plane (SH sensor)

$$U(u, v, L) = \frac{e^{ikz}}{i\lambda z} e^{\frac{ik}{2z}(u^2+v^2)} \mathcal{F}[U(x, y, 0)]. \quad (5-3)$$

Notice that the last equations correspond to Eq. (A-11) and (A-13), respectively. The Fourier transform and its inverse were introduced to ease the implementation of the simulation.

Adapt to accommodate two different coordinate pairs: (x,y) refers to the pupil plane; (u,v) refers to the focal/propagation plane.

The phase Φ can be parametrized as a linear combination of K general basis functions f_k .

$$\Phi(x, y) = \sum_{k=1}^K \alpha_k f_k(x, y) \quad (5-4)$$

These coefficients α_k can be estimated by minimizing the error between the intensity of the field given by the model and the measured intensity. Let $I_{\text{meas}}(x_i, y_j)$ represent the measured intensities of each pixel (i, j) at the detection plane and let $I(x_i, y_j, L) = |U(x_i, y_j, L)|^2$ be the intensity given by the physical model also evaluated in pixel (i, j) . With these two quantities one is able to define a simple cost function (Eq. (5-5)). For the sake of simplicity, the plane defined by the variables (x, y) will be sampled in such a way that (x_i, y_j) correspond to the center of the pixel (i, j) .

$$J = \sum_{i,j} [I_{\text{meas}}(x_i, y_j) - I(x_i, y_j, L)]^2 \quad (5-5)$$

In [5] a nonlinear least squares optimization procedure was performed to estimate the coefficients α_k that describe the phase distribution (5-4). In the next section, we linearise the model so that the phase-retrieval problem can be solved using a least-squares approach instead of a non-linear method.

Formulation of the linearised problem

replace all m by x, y

Firstly, both $I_{\text{meas}}(x_i, y_j)$ and $I(x_i, y_j, L)$ in (5-5) are vectorized such that, given a total of M pixels, two vectors \mathbf{i}_{meas} and $\mathbf{i}_L \in \mathbb{R}^{M \times 1}$ are created. Thus, a new cost function J_{vec} can then be defined.

$$J_{\text{vec}} = \|\mathbf{i}_{\text{meas}} - \mathbf{i}_L\|_2^2 \quad (5-6)$$

$$= \sum_{m=1}^M (F(m) - I(m, L))^2 \quad (5-7)$$

Note that each element m of the newly created vectors has a direct mapping to a point (x_i, y_j) in the Cartesian plane.

In order to find the coefficients that minimize J_{vec} using a linear method, we linearise the intensity term defined at a certain pixel $I_L(m) = I(m, L)$ using a first-order Taylor series around an arbitrary vector of phase coefficients $\tilde{\alpha}$. In this case we will use $\tilde{\alpha} = 0$.

$$I_L(m) = U_L^*(m)U_L(m) \quad (5-8)$$

$$\frac{\partial I_L(m)}{\partial \boldsymbol{\alpha}} = \left[\frac{\partial U_L^*(m)}{\partial \boldsymbol{\alpha}} U_L(m) + U_L^*(m) \left(\frac{\partial U_L(m)}{\partial \boldsymbol{\alpha}} \right) \right] \quad (5-9)$$

The truncated first-order Taylor can then be expressed as follows:

$$\begin{aligned} I_L(m) &\approx I_L(m)_{\boldsymbol{\alpha}=\hat{\boldsymbol{\alpha}}} + \left[\frac{\partial U_L^*(m)}{\partial \boldsymbol{\alpha}} U_L(m) + U_L^*(m) \frac{\partial U_L(m)}{\partial \boldsymbol{\alpha}} \right]_{\boldsymbol{\alpha}=\hat{\boldsymbol{\alpha}}} \boldsymbol{\alpha} \\ &= c_{0m} + \mathbf{c}_{1m} \boldsymbol{\alpha} \end{aligned} \quad (5-10)$$

where

$$\frac{\partial U_L(m)}{\partial \boldsymbol{\alpha}} = \begin{bmatrix} \frac{\partial U_L(m)}{\partial \alpha_1} & \dots & \frac{\partial U_L(m)}{\partial \alpha_K} \end{bmatrix} \in \mathbb{R}^{1 \times K}$$

$$\frac{\partial U_L(m)}{\partial \alpha_k} = \mathcal{F}^{-1} [\mathcal{F}[U_0(m) i \nu f_k(m)] H(m)] \quad (5-11)$$

The details about the implementation can be found in [55].

The terms c_{0m} and \mathbf{c}_{1m} in Eq. (5-10) are computed for each $m = 1, \dots, M$ in order to define $\mathbf{c}_0 = [c_{01}, \dots, c_{0M}]^T \in \mathbb{R}^{M \times 1}$ and $\mathbf{C}_1 = [\mathbf{c}_{11}^T, \dots, \mathbf{c}_{1M}^T] \in \mathbb{R}^{M \times K}$. This new formulation is helpful in order to present the new cost function J_{lin} for the linearized problem:

$$\text{minimize } J_{\text{lin}} = \|\mathbf{i}_{\text{meas}} - (\mathbf{c}_0 + \mathbf{C}_1 \boldsymbol{\alpha})\|_2^2 \quad (5-12)$$

The optimal solution for this problem is then:

$$\hat{\boldsymbol{\alpha}} = (\mathbf{C}_1^T \mathbf{C}_1)^{-1} \mathbf{C}_1^T (\mathbf{c}_0 - \mathbf{i}_{\text{meas}}) \quad (5-13)$$

The information in this section together with Chapter 3 on B-splines provide the framework to solve the problem at hand.

Subaperture local problem

In this phase retrieval method, we propose that both the pupil and detection planes are divided in N (where N is the number of subapertures) equal and adjacent square regions. Each cell in the pupil plane contains one subaperture. Each cell in the detection plane corresponds to the area that "sees" the local wavefront sampled by a subaperture. We will use the data from the subimage on the detection plane to estimate the phase only in its corresponding subaperture.

Image showing this division with both planes

Provided that the diffraction effects on the detection plane are small, one can guarantee that the propagated beams from one subaperture have a minimal effect in the subimage corresponding to another subaperture. Therefore, the linear optimization procedure defined in (5-12) can be applied locally and almost independently to estimate the phase distribution in each of the subapertures.

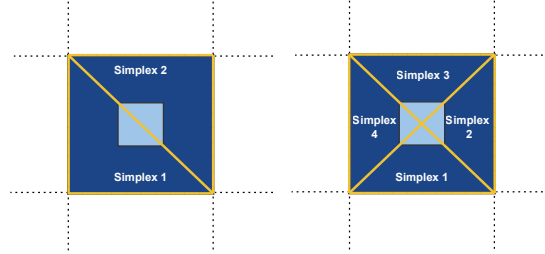


Figure 5-1: Close-up on one of the subapertures. In the left (right) subaperture a type I (II) triangulation was defined using 2 (4) simplices per subaperture

The local areas that have been defined in both planes are square whereas the B-splines are defined in a simplex with a triangular shape. Therefore, the phase distribution was parametrized using J triangles that divide the subaperture. An example with 2 (type I triangulation) and 4 (type II triangulation) can be seen in Figure 5-1.

In order to ensure continuity in the same subaperture one may enforce the continuity constraints (Eq. (3-15)) inherent to the spline framework. The word may is used as these constraints are not nearly as important as the ones that connect the different subapertures which will be presented in the next section. The formulation of the local problem is presented in (5-14) for a certain aperture n .

$$\begin{aligned}
 & \text{minimize} \quad \left\| \begin{bmatrix} \mathbf{i}_{\text{meas},1}^n \\ \vdots \\ \mathbf{f}_{\text{meas},J}^n \end{bmatrix} - \begin{bmatrix} \mathbf{c}_{0,1}^n \\ \vdots \\ \mathbf{c}_{0,J}^n \end{bmatrix} - \begin{bmatrix} \mathbf{C}_{1,11}^n & \cdots & \mathbf{C}_{1,1J}^n \\ \vdots & \ddots & \vdots \\ \mathbf{C}_{1,J1}^n & \cdots & \mathbf{C}_{1,JJ}^n \end{bmatrix} \begin{bmatrix} \alpha_1^n \\ \vdots \\ \alpha_J^n \end{bmatrix} \right\|_2^2, \\
 & \text{subject to} \quad \mathbf{H}^{\text{local}} \begin{bmatrix} \alpha_1^n \\ \vdots \\ \alpha_J^n \end{bmatrix} = 0.
 \end{aligned} \tag{5-14}$$

Global optimization

The natural extension to Eq. (5-14) is to perform this optimization for all the subapertures simultaneously. For the optimization to be successful it is not enough to purely replicate the procedure presented in Eq. (5-12). Additional boundary constraints must be inserted in addition to those that provide continuity between the two neighbouring polynomials in each of the subapertures.

Let us provide an example. Take, for instance, the upper simplex in the left subaperture in Figure 5-1. Assuming that the adjacent subapertures have the same simplex layout, continuity constraints should be imposed to connect the aforementioned simplex with the lower simplices of the subapertures which are located upwards and to the right. These constraints should also be included in the smoothness matrix \mathbf{H} so as to generate a global problem for N subapertures.

$$\begin{aligned} \min \quad & \left\| \begin{bmatrix} \mathbf{i}_{\text{meas}}^1 \\ \vdots \\ \mathbf{i}_{\text{meas}}^N \end{bmatrix} - \left(\begin{bmatrix} \mathbf{c}_0^1 \\ \vdots \\ \mathbf{c}_0^N \end{bmatrix} + \mathbf{C}_1^{\text{global}} \begin{bmatrix} \boldsymbol{\alpha}^1 \\ \vdots \\ \boldsymbol{\alpha}^N \end{bmatrix} \right) \right\|_2^2, \\ \text{s.t.} \quad & \mathbf{H}^{\text{global}} \begin{bmatrix} \boldsymbol{\alpha}^1 \\ \vdots \\ \boldsymbol{\alpha}^N \end{bmatrix} = 0. \end{aligned} \quad (5-15)$$

where,

$$\mathbf{C}_1^{\text{global}} = \begin{bmatrix} \mathbf{C}_1^1 & & \\ & \ddots & \\ & & \mathbf{C}_1^N \end{bmatrix}$$

The solution for this problem can be found in an iterative or direct way as described in [39, Section 4.2].

5-1-2 Simulation Results

Demonstration of Operation of the new method

In this section, the performance of our our method is compared against a modal wavefront reconstruction algorithm presented in [28]. The principle of operation of this modal reconstruction method is explained in Section 2-3-2. The centroid algorithm used to compute the slope measurements is presented in [52].

no reference to this Figure?

The wavefront sensing setup simulated is similar to the one presented in [5]. A Hartmann wavefront sensor was simulated where each hole has a side length of $200 \mu\text{m}$ and is separated from the adjacent hole by a distance of $562.5 \mu\text{m}$. The propagation distance (i.e., the distance between the aperture plane and the detection plane) is 10 mm and the wavelength is $\lambda = 638 \text{ nm}$. A Hartmann grid of 10 by 10 subapertures was used.

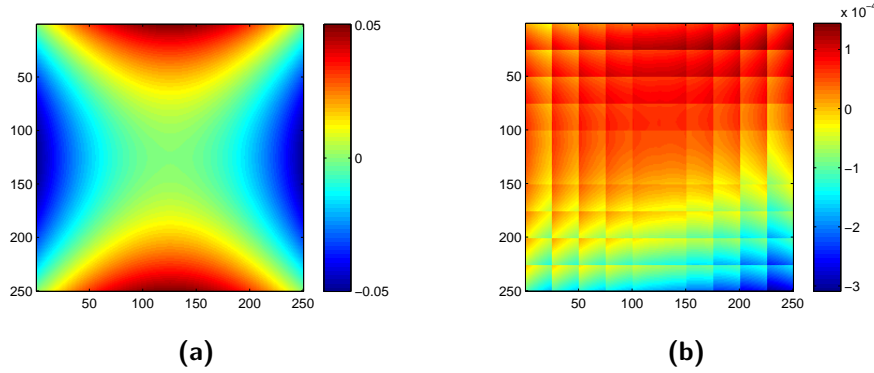


Figure 5-2: (a) Reconstructed phase distribution for $\alpha_4 = 0.1\lambda$ and (b) its error (both normalized to the wavelength λ) when the intensity distribution was subject to noise ($\sigma = 4 \times 10^{-4}$)

The sensor was considered to suffer predominantly the effects of read-out noise on the CCD camera. This noise was modelled as white and Gaussian with zero-mean and standard deviation $\sigma_{\text{ccd}} = 4 \times 10^{-4}$. The noise is additive and affects the normalized (between 0 and 1) intensity distribution values.

A 4th order Zernike mode (according to Noll notation [56]) was used to model the incoming wavefront. The polynomial functions of the B-splines were chosen to have a degree $d = 2$ and subject to continuity constraints of order $r = 2$. A type II triangulation partitions the subapertures, as per Figure 5-1.

The results presented in Figure 5-3 show that our method yields an RMS error approximately 1 order of magnitude lower in relation to the modal reconstruction method in the presence of noise for aberrations smaller than λ . In the noiseless case and for aberrations smaller than 0.1λ this method is able to provide an improvement of 2 orders of magnitude. For aberrations larger than 10λ , the diffraction pattern pertaining to a subaperture will affect the intensity pattern originating from other subapertures. In that case, our locality assumption is not verified and the method does not yield good results. It performs even poorer than the modal reconstruction for $\alpha_4 \geq 100\lambda$.

can I implement the splines algorithm using the non-linear model to see how much is lost due to the linearization?

For incoming wavefronts modelled using high frequency Zernike modes the method presents results with the same accuracy as presented in Figure 5-3 provided that the degree of the spline functions is increased. That is due to the fact that the Zernike basis functions have a polynomial term in terms of the radius. The degree of that term is called the radial degree and in order to approximate it correctly the splines polynomials must have at least the same degree. For example, if we wanted to approximate Zernike modes accurately from the 7th until the 10th (radial degree equals 3) we would have to choose at least a spline degree $d = 3$. To filter out the noise the continuity constraints should be of the same order, that is, $r = 3$.

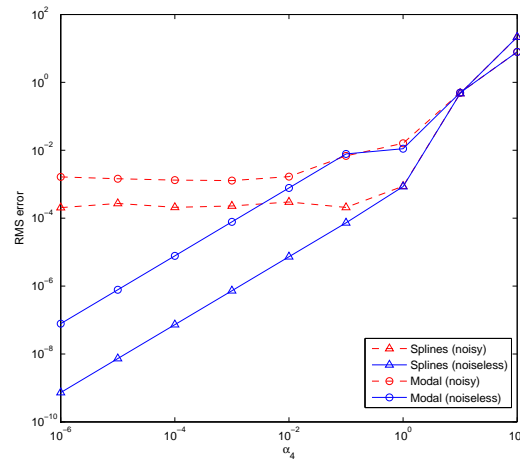


Figure 5-3: Comparison of the RMS of the wavefront reconstruction between the new spline based WFR method and the modal reconstruction method (in open-loop). It is clear that due to the influence of the noisy measurements the RMS values reach a threshold when the aberrations get smaller: around $1.5 \times 10^{-3}\lambda$ for modal reconstruction and $2.5 \times 10^{-4}\lambda$ for spline-based reconstruction. Other experiments were done with different incoming wavefronts and the results were similar to the one presented above.

Closed loop comparison

So far, the results presented only concerned the open-loop reconstruction where no feedback loop nor deformable mirror is included. In this section, the methods used previously for wavefront reconstruction were integrated in a classical AO feedback loop (Figure 5-4) in order to analyse the convergence properties and sensitivity to noise of the wavefront reconstruction error.

The closed-loop setup includes the wavefront sensor and the reconstruction algorithm with the same characteristics specified in Sec. 5-1-2. It also includes the deformable mirror, which in this case is assumed to be perfect, meaning that it will take the exact shape of the reconstructed wavefront. Furthermore, a delay was added in the loop simulating the time consumed by the computations and communications in a real-time implementation. A PI controller was also integrated and tuned in order to minimize the effect of the delay.

Using a wavefront characterized by an astigmatism aberration with a coefficient of 0.1λ we obtain the results presented in Figure 5-5.

With this approach the reconstruction error converges to a lower RMS value and is less sensitive to noise than the closed loop with modal reconstruction. In the presence of noise the modal reconstruction method can not achieve the threshold for small aberrations in open-loop that is visible in Figure 5-3, while our method can.

5-1-3 Conclusions

This novel wavefront reconstruction method represents a successful replacement for the classical slope measurement phase retrieval techniques. This linear method provides an improve-

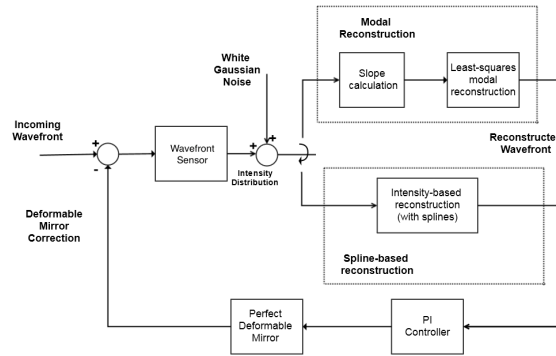


Figure 5-4: Simplified representation of a feedback loop used in Adaptive Optics

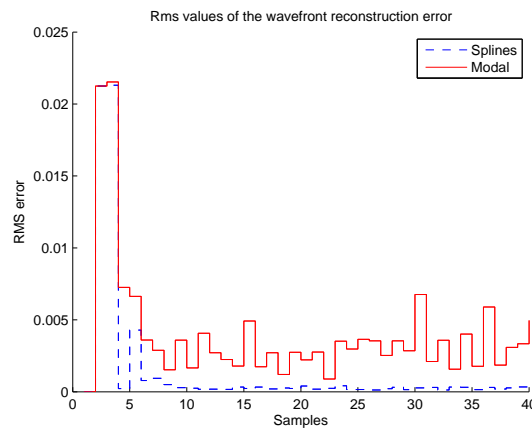


Figure 5-5: RMS error evolution for a classical AO setup comparing the modal and the spline-based reconstruction method.

ment of approximately one order of magnitude in terms of RMS error regarding the classical methods for aberrations smaller than λ . Besides that it is capable of approximating high frequency Zernike with the same accuracy as presented in Figure 5-3 for the low frequency mode, provided that the degree of the approximating splines is chosen to match that of the radial degree of the Zernike mode. Moreover, given the structure of the (Shack-)Hartmann sensor the problem has the potential to be solved in a distributed way.

From an AO control perspective, this method can be easily implemented in real-time feedback setups given its linearity. Besides that, integrating it in a classical AO feedback loop will yield a lower reconstruction error in all the cases mentioned in the previous paragraph provided that the deformable mirror has sufficient resolution to depict accurately the reconstructed phase.

5-2 Compressive sampling using Jacobian analysis

To guarantee real time applicability of the spline based method presented in the previous section with intensity measurements, we propose two approaches to reduce the computational

complexity. [35] have shown that the local nature of the B-spline framework allows highly distributed computation of the LS estimate. This method has been implemented for spline based wavefront reconstruction from slope measurements and can be extended to the method discussed in this section. In addition to the distributed implementation for speeding up, a second strategy based on compressive sensing [57] to further speed up improvements can be implemented. In this section, we focus on the latter improvement. We present simulation results which show that the number of pixels used for estimation of the wavefront can be reduced dramatically without significant loss of accuracy and robustness of the reconstruction.

5-2-1 Acceleration study through compressive sampling

Motivated by the work of [58] and others, who applied principles of the theory of compressive sensing and sampling to solve the phase retrieval problem, the idea is to only use $M' := \frac{cr}{100} M$ for $0 < cr \leq 100$, of the total number of M given intensity measurements stored in $\mathbf{i}_{\text{meas}}^{\text{glob}}$ to estimate the spline coefficients. This is implemented by introducing a selection matrix $\mathbf{S} \in \mathbb{R}^{M' \times M}$ in the cost function of the global reconstruction problem in (5-22), which yields a new cost function

$$j_{\text{lin}}^{\text{CS}} = \|\mathbf{S}(\mathbf{i}_{\text{meas}}^{\text{glob}} - \mathbf{c}_0^{\text{glob}}) - \mathbf{S}\mathbf{C}_1^{\text{glob}}\boldsymbol{\alpha}^{\text{glob}}\|_2^2. \quad (5-16)$$

Parameter cr denotes the undersampling of the intensity images and is further referred to as compression ratio. The LS estimate of the B-coefficient vector is then computed as

$$\boldsymbol{\alpha}^* = \mathbf{N}_{\mathbf{H}}(\mathbf{C}_1^{\text{CS}\text{T}}\mathbf{C}_1^{\text{CS}})^{-1}\mathbf{C}_1^{\text{CS}\text{T}}(\mathbf{i}_{\text{meas}}^{\text{glob}} - \mathbf{c}_0^{\text{glob}}), \quad (5-17)$$

where $\mathbf{C}_1^{\text{CS}} := \mathbf{S}\mathbf{C}_1^{\text{glob}}\mathbf{N}_{\mathbf{H}} \in \mathbb{R}^{M' \times k_H}$ with k_H denoting the nullspace dimension of constraint matrix \mathbf{H} .

Choosing at each time instance, the $M'_s = crM_s$ largest intensities in each subaperture of the sensor would guarantee maximal signal to noise ratio. However, this approach is not feasible for real time computations as it would turn the selection matrix \mathbf{S} to become time variant. The consequence of this is that the reconstruction matrix \mathbf{R} can no longer be pre-computed, thereby increasing the real-time computational complexity (unacceptably for large scale problems such as for extreme large telescopes). Two time-invariant procedures to construct a precomputed selection matrix \mathbf{S} are considered here. The first is inspired by the random sampling often performed in compressive sampling [57]. This results in determining \mathbf{S} such that at each time instance an identical (though a priori determined random) selection of M'_s pixels is made in each subaperture. The selection can differ for different subapertures. The second option is to choose the M'_s intensity measurements which are most “favoured” by the linear model in the following manner: For each subaperture n we determine a vector $\mathbf{k}_n \in \mathbb{R}^{M_s}$ as

$$\mathbf{k}_n(m) = \sum_{j=1}^K |\mathbf{C}_1^n(m, j)|, \quad (5-18)$$

for $m = 1, \dots, M_s$. The entries of this vector reflect the averaged (in terms of the ℓ_1 -norm) sensitivity of the intensity measurements to the spline coefficients corresponding to a local aperture. The selection matrix $\mathbf{S}_n \in \mathbb{R}^{M'_s \times M_s}$ is in this second option constructed such that

the M'_s pixels $i_{\text{meas}}^n(m)$ with the highest values for $\mathbf{k}_n(m)$ are selected. The global block diagonal selection matrix is given by

$$\mathbf{S} = \begin{bmatrix} \mathbf{S}_1 & & \\ & \ddots & \\ & & \mathbf{S}_N \end{bmatrix} \in \mathbb{R}^{M' \times M}. \quad (5-19)$$

For a regular triangulation with B-spline polynomials of same degree d used in all simplices the local matrices \mathbf{S}_n are identical for all $n = 1, \dots, N$. The motivation for the second selection option is that the “most sensitive” pixels will also be those that have the best signal to noise ratio. This heuristic argument will be further illustrated in the experimental section 5-2-2 where a significant advantage of the Jacobian based over the randomly computed selection matrix is shown.

5-2-2 Numerical Simulations

For the simulations, the same setup was used as in Section 5-1-2. An astigmatism, the 4th Zernike mode in Noll’s notation, is used to model the incoming wavefront with small aberrations of $\alpha_4 = 0.1\lambda$ where α_4 denotes the 4th Zernike coefficient. It was shown by [59] that the spline based method for intensity measurements provides stable results for aberrations smaller than λ . The wavefront is estimated on the aperture plane of the Hartmann sensor, where each subaperture is covered by 4 simplices. The phase screen is then approximated with a B-form polynomial of degree $d = 2$, subject to continuity constraints of order $r = 2$. To evaluate the performance of the wavefront reconstruction the RMS values of the residual wavefront, the difference between the simulated and the estimated phase screen (both normalised to the wavelength λ), have been computed for several noise realisations to obtain an averaged result.

Selection matrix and computational gain

In this section, the advantage of the Jacobian based selection matrix \mathbf{S} over its randomly computed counterpart is shown. It becomes especially significant for the compression ratios of interest $cr < 20\%$. Furthermore, a short complexity analysis of the real time computations which have to be performed in the presented reconstruction method shows the acceleration achieved with the compressive sampling approach.

is the computational complexity correctly drawn? In Figure 5-6, the RMS values of the normalised residual wavefront are plotted in logarithmic scale for wavefront estimates computed with $cr\%$ of the noisy CCD image pixels simulated for the described Hartmann set up and an astigmatic incoming wavefront. One can see, that the accuracy of the estimation performed for randomly selected pixels decreases already for less than 20% of compression ratio, where as the Jacobian based selection matrix provides stable results up to 10% and shows a steep increase in the RMS error only at a compression ratio of 1%. Even though these results do not replace a full analysis of the Jacobian based selection, they give sufficiently strong indication to use this approach for the compressive sampling.

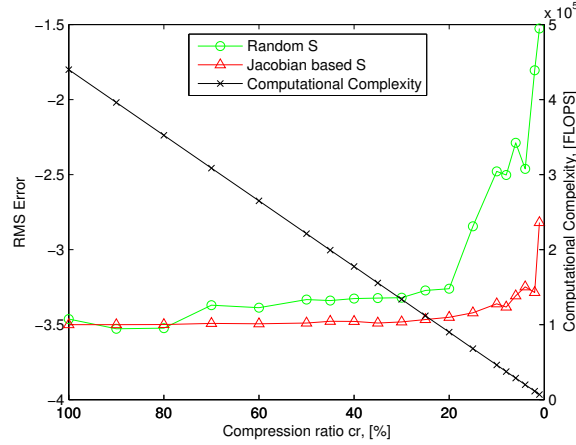


Figure 5-6: RMS errors between the reconstructed and the original 4th order Zernike wavefront for decreasing percentage $cr\%$ of intensity measurements used. Triangles: Randomly computed selection matrix. Circles: Jacobian based selection matrix. Crosses: Real time computational complexity depending on $cr\%$.

Next to the evolution of the RMS error, the computational complexity of the real time computations, which have to be performed in order to obtain the values of the estimated wavefront at N' point stacked in coordinate vector $\mathbf{x} \in \mathbb{R}^{N' \times 2}$, is shown in Figure 5-6 for decreasing compression ratio cr . This real time computation consists of the following 3 steps:

$$\phi^*(\mathbf{x}) = (\mathbf{B}(\mathbf{x})\mathbf{N}_H)(\mathbf{C}_1^{\text{CS}})^+ \mathbf{S}(\mathbf{i}_{\text{meas}}^{\text{glob}} - \mathbf{c}_0^{\text{glob}}), \quad (5-20)$$

where the product of the spline evaluation matrix $\mathbf{B}(\mathbf{x})$ and the nullspace projector \mathbf{N}_H as well as the pseudo inverse of the modified Jacobian \mathbf{C}_1^{CS} (introduced in (5-17)) are pre-computed. The selection of M' intensities with sparse matrix \mathbf{S} and the subtraction of the respective linearization offsets can be scaled at M' FLOPs (Floating Point Operations). The computational complexity is then given by

$$\mathcal{C} = (N'k_H + k_H M' + M') \text{FLOPs},$$

where the compressed total number of intensity measurements is $M' = cr M_s N$, with $M_s = 625$ pixels per subaperture and $N = 100$ subapertures in the considered case. Note that for a real case scenario of an extremely large telescope N scales at $\mathcal{O}(10^4)$. The real time computation is applied in the described way as dimension k_H of the nullspace of constraint matrix \mathbf{H} is much smaller than K and M' . k_H is a function of the total number of simplices and internal edges in the triangulation as well as degree d and continuity order r of the spline model[34] and equals 6 for the chosen setup and model. For p evaluation points per subaperture the computational complexity is obtained with

$$\mathcal{C} = (p k_H N + (k_H + 1) M_s N cr) \text{FLOPs}$$

as linearly decaying function of compression ratio cr , which is plotted for $p = 4$ evaluation points per subaperture in Figure 5-6.

Open loop comparison

In the following section, we present simulation results for open loop reconstruction which show that the spline based method for intensity measurements with compressive sensing of ratio $cr = 10\%$ suffers only minor to negligible losses in performance to variations in aberration strength and to different noise standard deviations, compared to the original method using the full CCD output. To allow further comparison to a standard wavefront reconstruction matrix, a modal wavefront reconstruction method using slope measurements was used for the same set up. For this very common method, the center of gravity of the intensity distribution is computed with the centroid algorithm for each subaperture of the Hartmann sensor. It approximates the averaged slopes of the wavefront seen by the respective subaperture. From these slope measurements the wavefront which is parametrized using Zernike polynomials can be estimated by solving the least squares problem for optimal weighting coefficients.

Figure 5-7 shows the RMS values of the absolute error maps between the estimated wavefront and the original incoming wavefront simulated by an astigmatism.

In the first plot, a fixed noise standard deviation was assumed while the open loop reconstructions were performed for varying aberration strength simulated by varying the Zernike weight α_4 . One can see that the spline and intensity based method give almost the same accuracy for reconstruction from 100% or 10% of the measurements. For aberrations smaller than λ the assumption of locally independent imaging holds and aberrations of higher polynomial orders can be retrieved from the intensity measurements. The centroid based method processes only information about the local slopes of the wavefront which yields a less accurate approximation. The RMS errors of both methods reach a threshold for very small aberrations due to the influence of the measurement noise. For aberrations larger than 10λ , the diffraction pattern corresponding to one subaperture affects the intensity pattern of the neighbouring such that the assumption for independent imaging is not valid anymore. In this case, slope measurements give better information about the shape of the wavefront.

The second plot shows the behaviour of the RMS error for the same simulations with a fixed $\alpha_4 = 0.1\lambda$ aberration where different noise levels on the intensity measurements were simulated. Again, the spline method shows the same behaviour using 10% of the intensity measurements as for reconstruction from all the pixels. Only a minor loss in accuracy was observed for the reduced version. Since the used spline polynomials of degree 2 cannot approximate higher modes in the wavefront, the performance reaches a limit due to fitting errors.

Closed loop comparison

In this section, the discussed wavefront reconstruction methods were integrated in a classical AO feedback loop. It is shown that the compressive sampling preserves the convergence properties and the sensitivity of the wavefront reconstruction error to noise of the spline and intensity based method.

The closed-loop setup includes a simulator of the Hartmann sensor specified at the beginning of Section 5-2-2 which computes the intensity measurements and models the read out and **photon noise**. The control loop configuration is the same as presented in Section 5-1-2.

Figure 5-8 shows the results obtained for an 0.1λ astigmatism aberration with measurement noise of standard deviation 10^{-4} . The splines based method reaches the same convergence

and noise sensitivity levels for compressed number of intensity measurements as for the full number of pixels. The RMS error values of the reconstruction error with the modal method using slope measurements emphasizes that the new intensity based spline approach converges to a lower error level and is less sensitive to noise than the classical method.

5-2-3 Conclusion

In this section, we introduced a procedure to accelerate the real time computation part of a recently presented wavefront reconstruction method for intensity measurements of a wavefront sensor without compromising the performance of the reconstruction. The novel compressive sensing reconstruction method significantly reduces the number of intensity measurements used for wavefront reconstruction to only a few percent of the full image information. First simulations of open-loop and closed-loop AO systems gave very promising results. This indicates that performance and robustness as well as the convergence gain that was established with the new intensity based reconstruction method [59] could be preserved with a significantly reduced computational complexity. The novel compressive sensing method is highly suitable for a distributed implementation, since the selection process is independently performed for each intensity pattern in the sensor's subapertures which stands in contrast to the globally applied random sampling in many compressive sensing methods. Due to the local nature of the presented compressive sensing reconstruction method for intensity measurements, it can be integrated with our recent work of [35] who have shown that the locally defined B-spline framework allows highly distributed computation of the LS wavefront estimate.

5-3 Distributed methods

The inherent structure of the wavefront reconstruction problem using a (Shack-)Hartmann sensor allow us to potentially formulate the problem in a distributed way. In this section the problem is presented in Sec. 5-3-1. Then the Alternating Direction Method of Multipliers (ADMM) is applied to solve the problem in Sec. 5-3-2. Finally the results are presented in Sec. 5-3-4.

5-3-1 Separable problem formulation

The wavefront reconstruction method presented in [59] and posed again in Section 5-1-1 is formulated as a linear least-squares problem subject to linear constraints.

$$\text{minimize} \quad \|\mathbf{i}_{\text{meas}} - (\mathbf{c}_0 + \mathbf{C}_1 \boldsymbol{\alpha})\|_2^2, \quad (5-21)$$

$$\text{subject to} \quad \mathbf{H} \boldsymbol{\alpha} = 0. \quad (5-22)$$

Due to the block diagonal structure of \mathbf{C}_1 the objective function can be split in N different functions, each pertaining to one subaperture.

$$\|\mathbf{i}_{\text{meas}} - (\mathbf{c}_0 + \mathbf{C}_1 \boldsymbol{\alpha})\|_2^2 = \left\| \mathbf{i}_{\text{meas}}^1 - \left(\mathbf{c}_0^1 + \mathbf{C}_1^1 \boldsymbol{\alpha}^1 \right) \right\|_2^2 + \cdots + \left\| \mathbf{i}_{\text{meas}}^N - \left(\mathbf{c}_0^N + \mathbf{C}_1^N \boldsymbol{\alpha}^N \right) \right\|_2^2 \quad (5-23)$$

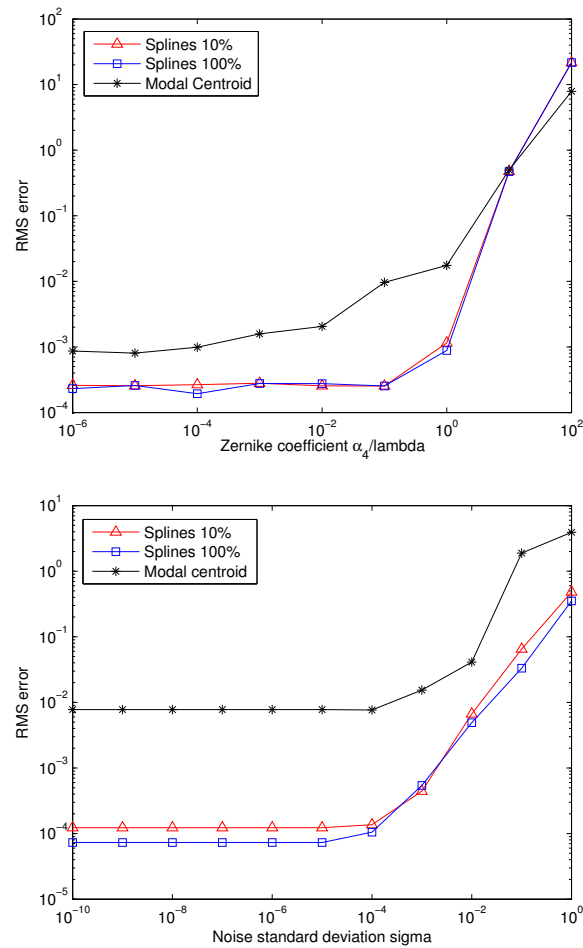


Figure 5-7: RMS errors for different reconstruction methods: Spline based method for 10% of the intensity measurements (Triangles), spline based method using all given intensity measurements (Squares), classical modal reconstruction method for slope measurements (Stars). Top: Fix noise standard deviation $\sigma_{ccd} = 4 \times 10^{-4}$, increasing aberration strength simulated by augmenting the Zernike coefficient α_4 . Bottom: Fix astigmatic aberration for $\alpha_4 = 0.1\lambda$, noise with varying standard deviation σ_{ccd} .

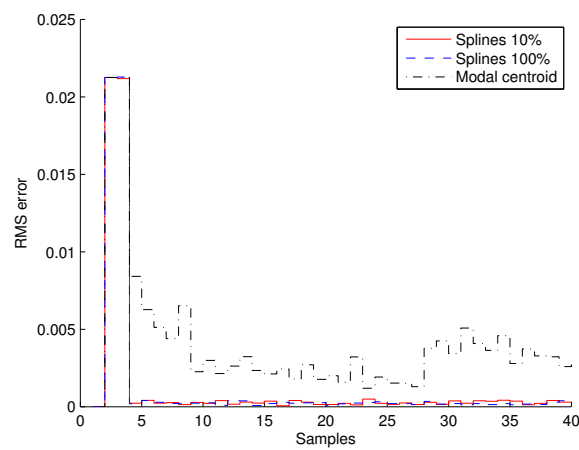


Figure 5-8: RMS value of the residual wavefront for a classical closed loop AO setup for reconstruction from intensities with the spline based method (Solid: 10% of pixels; Dashed: all pixels) and from slopes with the classical modal method (Dot-dashed).

The constraints can also be separated according to the subapertures by selecting the columns associated with each set of variables.

$$\mathbf{H}\boldsymbol{\alpha} = \begin{bmatrix} \mathbf{H}^1 & \dots & \mathbf{H}^N \end{bmatrix} \begin{bmatrix} \boldsymbol{\alpha}^1 \\ \vdots \\ \boldsymbol{\alpha}^N \end{bmatrix} = 0 \quad (5-24)$$

Hence the full problem separated in the coefficients that belong to each of the subapertures can be written as follows:

$$\begin{aligned} \text{minimize } & \|\mathbf{i}_{\text{meas}} - (\mathbf{c}_0 + \mathbf{C}_1\boldsymbol{\alpha})\|_2^2 = \|\mathbf{i}_{\text{meas}}^1 - (\mathbf{c}_0^1 + \mathbf{C}_1^1\boldsymbol{\alpha}^1)\|_2^2 + \dots + \|\mathbf{i}_{\text{meas}}^N - (\mathbf{c}_0^N + \mathbf{C}_1^N\boldsymbol{\alpha}^N)\|_2^2 \\ \text{subject to } & \begin{bmatrix} \mathbf{H}^1 & \dots & \mathbf{H}^N \end{bmatrix} \begin{bmatrix} \boldsymbol{\alpha}^1 \\ \vdots \\ \boldsymbol{\alpha}^N \end{bmatrix} = 0 \end{aligned} \quad (5-25)$$

The objective is, thus, to find a method that enable us to solve this problem in a distributed way. The next section illustrates the use of ADMM to solve the problem.

5-3-2 ADMM application to wavefront reconstruction

The problem described in Eq. (5-25) can be seen as a slightly more involved version of the canonical exchange problem presented in Section 4-3-1.

$$\boldsymbol{\alpha}_i^{k+1} = \underset{\boldsymbol{\alpha}_i}{\text{argmin}} \left(\left\| \mathbf{f}^i - (\mathbf{c}_{0i} + \mathbf{C}_{1i}\boldsymbol{\alpha}_i) \right\|_2^2 + \mathbf{y}^{kT} \mathbf{H}_i \boldsymbol{\alpha}_i + (\rho/2) \left\| \mathbf{H} \begin{bmatrix} \boldsymbol{\alpha}_1^k \\ \vdots \\ \boldsymbol{\alpha}_i \\ \vdots \\ \boldsymbol{\alpha}_N^k \end{bmatrix} \right\| \right) \quad (5-26)$$

$$\mathbf{y}^{k+1} = \mathbf{y}^k + \rho \mathbf{H} \boldsymbol{\alpha}^{k+1} \quad (5-27)$$

The derivations needed to obtain the update formulas presented next can be found in Appendix B.

The $\boldsymbol{\alpha}_i$ updates can be done completely in parallel for each iteration. After one iteration the results are joined and a central operation to update the dual variable \mathbf{y} is performed. This update tries to maximize the dual variable by following the gradient of the augmented Lagrangian with respect to the dual variable weighted by ρ . This gradient is simply given by $\boldsymbol{\alpha}^{k+1}$.

5-3-3 Further improvements

For an improvement in convergence speed one can make the factor ρ adaptative. For that several mechanisms are available, the simplest one being: when the value $\|\mathbf{H}\boldsymbol{\alpha}\|$ in iteration $k + 1$ increases in relation to the value of iteration k (which means that we are diverging from the objective in what the constraints are concerned) the ρ is made bigger. Otherwise its value is decreased.

5-3-4 Results

The results will be presented with the open-loop specifications of the simulation setup used in [59]. The incoming wavefront is an 4-th order Zernike polynomial (according to Noll notation).

Modal	Splines		
Zernike	Centralized	D-SABRE	ADMM
6.90×10^{-3}	2.05×10^{-4}	8.63×10^{-4}	4.81×10^{-4}

Table 5-1: Wavefront reconstruction RMS errors normalized to the wavelength average over 5 different noise distributions. Both the dual ascent in D-SABRE and the ADMM implementation were run for 500 iterations with no stopping criterion

This shows that this method can obtain a significantly better performance than D-SABRE maintaining the linearity of the method and simplifying its general structure.

Due to the fact that the communication needed between the different simplices is very simple and well structured the implementation in a GPU of such a method would surely bring improvements for real-time Adaptive Optics systems.

Thesis Goal and Research Approach

6-1 Thesis Goal

The main objective of the thesis that this literature survey precludes is the creation of high-accuracy and distributable wavefront reconstruction algorithms. Their properties in terms of noise propagation, reconstruction performance and computational complexity will be analysed and compared.

6-2 Research Approach

To accomplish the main objective, several other steps must be taken. The order in which these steps are presented here is not necessarily chronologically due.

1. compare the noise properties of intensity based and classical reconstruction methods.
2. apply the novel method to the experimental setup in the laboratory.
3. apply the method for flight formation in [60] to distributed wavefront reconstruction.
4. analyse the computational complexity of the distributed methods.
5. devise a GPU implementation for the best performing distributed method.

Appendix A

Model of the Shack-Hartmann Wavefront Sensor

A-1 Intensity Distribution model

The deductions in this section were based mainly on Chapters 3 to 5 of [54] and the work done in [61].

When using model-based wavefront reconstruction algorithms, the model chosen must be as accurate as possible. To this end, one must fully understand how to derive implementable algorithms (such as the ones in [55] and [62]) from plain Maxwell's equations so that all approximations and assumptions are taken into consideration.

The first step is, then, to write Maxwell's equations in the absence of free charge and free current

$$\nabla \times \mathbf{E} = -\mu \frac{\partial \mathbf{H}}{\partial t} \quad (\text{A-1})$$

$$\nabla \times \mathbf{H} = \epsilon \frac{\partial \mathbf{E}}{\partial t} \quad (\text{A-2})$$

$$\nabla \cdot \epsilon \mathbf{E} = 0 \quad (\text{A-3})$$

$$\nabla \cdot \mu \mathbf{H} = 0, \quad (\text{A-4})$$

where \mathbf{E} represents the electric field and \mathbf{H} the magnetizing field.

ambiguity regarding the meaning of ϵ and μ with respect to their previous usage.

Before proceeding with the derivations some properties of the medium must be explicated.

- the medium is *linear* if it does not change its properties due to the intensity of the light.

- the medium is *isotropic* when its properties do not depend on the direction of the fields.
- *homogeneity* guarantees that the permittivity ϵ of the medium is constant.
- the medium is *non-dispersive* if it does not depend on the wavelength region of the wave.
- finally, a medium is *non-magnetic* when the permeability μ equals the permeability in vacuum μ_0 .

If all of these properties are verified (or assumed to be verified) one can decouple each of the components of the fields \mathbf{E} and \mathbf{H} from one another and, thus, write the following expression

$$\nabla^2 u(\mathbf{x}, t) - \frac{n^2}{c^2} \frac{\partial^2 u(\mathbf{x}, t)}{\partial t^2} = 0, \quad (\text{A-5})$$

where the scalar term u can be replaced by any of the components of \mathbf{E} or \mathbf{H} . The vector $\mathbf{x} \in \mathbb{R}^3$ represents the position. The refractive index of the medium is given by n and the velocity of light propagation by c .

For a monochromatic wave we can write

$$u(\mathbf{x}, t) = A(\mathbf{x}) \cos(2\pi\nu t + \phi(\mathbf{x})), \quad (\text{A-6})$$

which can be also written as

$$u(\mathbf{x}, t) = \text{Re}\{U(\mathbf{x}) \exp(-j2\pi\nu t)\}, \quad (\text{A-7})$$

$$U(\mathbf{x}) = A(\mathbf{x}) \exp(-i\phi(\mathbf{x})), \quad (\text{A-8})$$

Equations (A-6) and (A-7) show that the time dependence can be dropped as it can be immediately retrieved from $U(\mathbf{x})$. Substituting Eq. (A-7) in (A-5) yields the Helmholtz equation in U

$$(\nabla^2 + k)U(\mathbf{x}) = 0, \quad (\text{A-9})$$

where $k = 2\pi/\lambda$ is the wavenumber.

The application of Green's theorem [54, Section 3.2.2] under the Rayleigh-Sommerfeld formulation of diffraction [54, Section 3.5] enable us to solve the Helmholtz equation in Eq. (A-9) in terms of the quantity U . The solution obtained is called the Huygens-Fresnel principle. For our purposes, we will consider that the propagation is done in the direction of the coordinate z . Furthermore, the electro-magnetic field in the diffracting aperture is defined in a plane (x, y) and the field after propagation in a parallel plane with its points parametrized by the coordinates (u, v) (similar notation as Eq. (2-5); Figure 2-3 may help visualize the planes to

which we refer). Given these parametrizations and imposed propagation conditions, we can write, without loss of generality the Huygens-Fresnel principle in rectangular coordinates

$$U(u, v) = \frac{z}{i\lambda} \iint U(x, y) \frac{e^{ikr}}{r^2} dx dy, \quad (\text{A-10})$$

where $r = \sqrt{z^2 + (u-x)^2 + (v-y)^2}$. The only assumption made is that the propagation distance z must be much bigger than λ so that we can consider far-field propagation.

Another approximation can be made to simplify Eq. (A-10) such that it can be evaluated analytically. The approximation is called the Fresnel approximation and it consists in truncating the term r^2 . The resulting expression is given by

$$U(u, v) = \frac{e^{ikz}}{i\lambda z} e^{\frac{ik}{2z}(u^2+v^2)} \iint U(x, y) e^{\frac{ik}{2z}(x^2+y^2)} e^{\frac{-2\pi i}{\lambda z}(ux+vy)} dx dy. \quad (\text{A-11})$$

When a lens is introduced, the phase of the light is changed due to the introduction of a medium with a different refractive index. The complex field immediately before and after the transmission through the lens can be described as follows

$$U_{\text{after lens}}(x, y) = e^{-\frac{ik}{2f}(x^2+y^2)} U_{\text{before lens}}(x, y). \quad (\text{A-12})$$

The exponential term provides the phase shift of a lens with a certain focal length f and with its optical axis aligned with the direction z . Note, however, that this expression describes accurately the lens only for (x, y) pairs close to the optical axis of the lens.

If we introduce the resulting complex field from (A-12) in (A-11) we have

$$U(u, v) = \frac{e^{ikz}}{i\lambda z} e^{\frac{ik}{2z}(u^2+v^2)} \iint U_{\text{before lens}}(x, y) e^{\frac{-2\pi i}{\lambda z}(ux+vy)} dx dy. \quad (\text{A-13})$$

Notice that the first exponential term is a constant phase shift and can thus be dropped. To obtain the intensity distribution $I(u, v)$ that appears in Eq. (2-5) we simply take the square of the magnitude of $U(u, v)$,

$$I(u, v) = |U(u, v)|^2. \quad (\text{A-14})$$

A-2 Slope model

The derivation presented stems from the one in [14].

Let us assume that the wavefront ideally is flat. The distance between the lenslet (or aperture) array is given by z . The displacement of the centroid regarding its ideal position, if the wavefront is aberrated, is given by Δx and Δy .

The wavefront can then be approximated as only a tilt and its slope may be computed as follows, provided that α_x and α_y are the degrees of the tilt:

$$\tan(\alpha_x) = \frac{\Delta x}{z} \quad (\text{A-15})$$

Using the small-angle approximation we have that $\tan(\theta) \approx \theta$, $\theta \approx 0$. Thus,

$$\alpha_x \approx \frac{\Delta x}{z} \quad (\text{A-16})$$

The same procedure can be replicated for the tilt in the y direction.

By multiplying by the distance z on both sides of Eq. (A-16) and considering the presence of noise we arrive at Eq.(2-4)

Appendix B

Auxiliar derivations to support ADMM method

This section provides a derivation to the minimization of the augmented Lagrangian $\mathcal{L}_{i,\rho}$ in Eq. (5-26). To perform the minimization one can set the Jacobian with respect to a certain α_i to zero.

$$\nabla_{\alpha_i} \mathcal{L}_{i,\rho} = \nabla_{\alpha_i} \left(\left\| \mathbf{f}^i - (\mathbf{c}_0^i + \mathbf{C}_1^i \alpha^i) \right\|_2^2 + \mathbf{y}^{kT} \mathbf{H}_i \alpha_i + (\rho/2) \left\| \mathbf{H} \begin{bmatrix} \alpha_1^k \\ \vdots \\ \alpha_i \\ \vdots \\ \alpha_N^k \end{bmatrix} \right\| \right) = 0 \quad (\text{B-1})$$

One can split the previous equation into three independent terms which can be analysed individually.

$$\nabla_{\alpha_i} \left(\left\| \mathbf{f}^i - (\mathbf{c}_0^i + \mathbf{C}_1^i \alpha^i) \right\|_2^2 \right) = 2\mathbf{C}_{1i}^T \mathbf{C}_{1i} \alpha_i - 2\mathbf{C}_{1i}^T \mathbf{c}_{0i} \quad (\text{B-2})$$

$$\nabla_{\alpha_i} (\mathbf{y}^{kT} \mathbf{H}_i \alpha_i) = \mathbf{H}_i^T \mathbf{y}^k \quad (\text{B-3})$$

$$\nabla_{\alpha_i} \left((\rho/2) \left\| \mathbf{H} \begin{bmatrix} \alpha_1^k \\ \vdots \\ \alpha_i \\ \vdots \\ \alpha_N^k \end{bmatrix} \right\| \right) = \rho \left(\mathbf{H}_i^T \mathbf{H}_i \alpha_i + \mathbf{H}_i^T \mathbf{H}_{\neq i} \alpha_{\neq i}^k \right) \quad (\text{B-4})$$

In the last equation a non-standard symbol needs explanation. The symbols $\mathbf{H}_{\neq i}$ and $\alpha_{\neq i}^k$ represent in the case of the former all the columns of matrix \mathbf{H} except those pertaining to

subaperture i and for the latter all the rows of the vector that do not parametrize the phase in the subaperture i .

The minimum value for $\boldsymbol{\alpha}_i$ can then be written as

$$\boldsymbol{\alpha}_i^{k+1} = (2\mathbf{C}_{1i}^T \mathbf{C}_{1i} + \rho \mathbf{H}_i^T \mathbf{H}_i)^{-1} (2\mathbf{C}_{1i}^T \mathbf{c}_{0i} - \mathbf{H}_i^T \mathbf{y}^k + \mathbf{H}_i^T \mathbf{H}_{\neq i} \boldsymbol{\alpha}_{\neq i}^k) \quad (\text{B-5})$$

Bibliography

- [1] W. H. Southwell, “Wavefront estimation from wavefront slope measurements,” *J. Opt. Soc. Am.*, vol. 70, pp. 998–1006, Aug. 1980.
- [2] F. Roddier, *Adaptive Optics in Astronomy*. Cambridge University Press, 1999.
- [3] Markus, K.-P., “Overall science goals and top level ao requirements for the E-ELT,” in *1st AO4ELT conference - Adaptive Optics for Extremely Large Telescopes* (T. F. Y. Clénét, J.-M. Conan and G. R. (Eds.), eds.), 2010.
- [4] P. Mercère, P. Zeitoun, M. Idir, S. L. Pape, D. Douillet, X. Levecq, G. Dovillaire, S. Bucourt, K. A. Goldberg, P. P. Naulleau, and S. Rekawa, “Hartmann wave-front measurement at 13.4 nm with $\lambda_{\text{euV}}/120$ accuracy,” *Opt. Lett.*, vol. 28, pp. 1534–1536, Sep. 2003.
- [5] A. Polo, V. Kutchoukov, F. Bociort, S. Pereira, and H. Urbach, “Determination of wave-front structure for a Hartmann Wavefront Sensor using a phase-retrieval method,” *Optics Express*, pp. 7822–7832, 2012.
- [6] H. W. Babcock, “The possibility of compensating astronomical seeing,” *Publications of the Astronomical Society of the Pacific*, vol. 65, pp. 229–236, Oct. 1953.
- [7] K. Hinnen, M. Verhaegen, and N. Doelman, “A data driven H2-optimal control approach for adaptive optics,” *IEEE Trans. on Control Systems Technology*, vol. 16, no. 3, pp. 381–395, 2008.
- [8] G. Rousset, J. C. Fontanella, P. Kern, and F. Rigaut, “First diffraction-limited astronomical images with adaptive optics,” *Astronomy and Astrophysics*, vol. 230, pp. L29–L32, Apr. 1990.
- [9] J. M. Beckers, “Adaptive optics for astronomy: Principles, performance, and application,” *Annual review of astronomy and astrophysics*, vol. 31, pp. 13–62, 1993.
- [10] M. Verhaegen, “Lecture notes on control for High Resolution Imaging,” May 2012.

- [11] B. Platt and R. Shack, "History and principles of shack-hartmann wavefront sensing," *J. of Refractive Surgery*, vol. 17, pp. 573–577, Sep./Oct. 2001.
- [12] W. Boyle and G. Smith, "Charge coupled devices," *Bell Syst. Tech. Journal*, vol. 49, pp. 587–593, 1970.
- [13] S. Tisa, F. Zappa, and S. Cova, "Monolithic quad-cells for single-photon timing and tracking," in *Society of Photo-Optical Instrumentation Engineers (SPIE) Conference Series*, vol. 6583 of *Society of Photo-Optical Instrumentation Engineers (SPIE) Conference Series*, May 2007.
- [14] Spiricon, ed., *Hartmann Wavefront Analyzer Tutorial*. Spiricon, 2004.
- [15] J. Ares and J. Arines, "Influence of thresholding on centroid statistics: Full analytical description," *Appl. Opt.*, vol. 43, pp. 5796–5805, Nov. 2004.
- [16] K. L. Baker and M. M. Moallem, "Iteratively weighted centroiding for Shack-Hartmann wave-front sensors," *Opt. Express*, vol. 15, pp. 5147–5159, Apr. 2007.
- [17] C. Leroux and C. Dainty, "Estimation of centroid positions with a matched-filter algorithm: relevance for aberrometry of the eye," *Opt. Express*, vol. 18, pp. 1197–1206, Jan. 2010.
- [18] S. Thomas, "Optimized centroid computing in a Shack-Hartmann sensor," *SPIE*, vol. 5490, pp. 1238 – 1246, 2004.
- [19] D. L. Fried, "Least-square fitting a wave-front distortion estimate to an array of phase-difference measurements," *J. Opt. Soc. Am.*, vol. 67, pp. 370–375, Mar. 1977.
- [20] R. H. Hudgin, "Wave-front reconstruction for compensated imaging," *J. Opt. Soc. Am.*, vol. 67, pp. 375–378, Mar. 1977.
- [21] C. R. Vogel, "Sparse matrix methods for wavefront reconstruction, revisited," vol. 5490, pp. 1327–1335, 2004.
- [22] E. Thiébaud and M. Tallon, "Fast minimum variance wavefront reconstruction for extremely large telescopes," *J. Opt. Soc. Am. A*, vol. 27, pp. 1046–1059, May 2010.
- [23] M. Rosensteiner, "Cumulative Reconstructor: fast wavefront reconstruction algorithm for extremely large telescopes," *J. Opt. Soc. Am. A*, vol. 28, pp. 2132–2138, Oct. 2011.
- [24] M. Rosensteiner, "Wavefront reconstruction for extremely large telescopes via CuRe with domain decomposition," *J. Opt. Soc. Am. A*, vol. 29, pp. 2328–2336, Nov. 2012.
- [25] K. R. Freischlad and C. L. Koliopoulos, "Modal estimation of a wave front from difference measurements using the discrete Fourier transform," *J. Opt. Soc. Am. A*, vol. 3, pp. 1852–1861, Nov. 1986.
- [26] L. A. Poyneer, D. T. Gavel, and J. M. Brase, "Fast wave-front reconstruction in large adaptive optics systems with use of the Fourier transform," *J. Opt. Soc. Am. A*, vol. 19, pp. 2100–2111, Oct. 2002.

-
- [27] J. Herrmann, “Least-squares wave front errors of minimum norm,” *J. Opt. Soc. Am.*, vol. 70, pp. 28–35, Jan. 1980.
 - [28] R. Cubalchini, “Modal wave-front estimation from phase derivative measurements,” *J. Opt. Soc. Am.*, vol. 69, pp. 972–977, Jul. 1979.
 - [29] L. Gilles, C. R. Vogel, and B. L. Ellerbroek, “Multigrid preconditioned conjugate-gradient method for large-scale wave-front reconstruction,” *J. Opt. Soc. Am. A*, vol. 19, pp. 1817–1822, Sep. 2002.
 - [30] Y. Saad, *Iterative Methods for Sparse Linear Systems*. Society for Industrial and Applied Mathematics, 2nd ed., 2003.
 - [31] C. R. Vogel and Q. Yang, “Multigrid algorithm for least-squares wavefront reconstruction,” *Appl. Opt.*, vol. 45, pp. 705–715, Feb. 2006.
 - [32] P. J. Hampton, P. Agathoklis, and C. Bradley, “A New Wave-Front Reconstruction Method for Adaptive Optics Systems Using Wavelets,” *IEEE Journal of Selected Topics in Signal Processing*, vol. 2, pp. 781–792, Nov. 2008.
 - [33] R. G. Lane, A. Glindemann, and J. C. Dainty, “Simulation of a Kolmogorov phase screen,” *Waves in Random Media*, vol. 2, no. 3, pp. 209–224, 1992.
 - [34] C. Visser and M. Verhaegen, “Wavefront reconstruction in adaptive optics systems using nonlinear multivariate splines,” *Journal of the Optical Society of America A*, vol. 30, no. 1, pp. 8295–8301, 2013.
 - [35] C. Visser and M. Verhaegen, “A distributed simplex B-splines based wavefront reconstruction,” 2012.
 - [36] M. Cayrel, “E-ELT optomechanics: overview,” in *Society of Photo-Optical Instrumentation Engineers (SPIE) Conference Series*, vol. 8444 of *Society of Photo-Optical Instrumentation Engineers (SPIE) Conference Series*, Sept. 2012.
 - [37] P. Massioni, R. Fraanje, and M. Verhaegen, “Adaptive optics application of distributed control design for decomposable systems,” in *Decision and Control, 2009 held jointly with the 2009 28th Chinese Control Conference. CDC/CCC 2009. Proceedings of the 48th IEEE Conference on*, pp. 7113–7118, 2009.
 - [38] P. Massioni, *Decomposition Methods for Distributed Control and Identification*. PhD thesis, Delft University of Technology, 2010.
 - [39] C. Visser, “Global nonlinear model identification with multivariate splines,” 2012.
 - [40] M. J. Lai and L. L. Schumaker, *Spline Functions on Triangulations*. Cambridge University Press, 2007.
 - [41] C. de Boor, “What is a multivariate spline?” in J. McKenna and R. Temam, editors, “*ICIAM ’87: Proceedings of the First International Conference on Industrial and Applied Mathematics*,” p. 90–101, 1987.
 - [42] L. E. Ghaoui, “Lectures for ee 227a: Convex optimization and applications,” Feb. 2012.

- [43] G. B. Dantzig and P. Wolfe, "Decomposition principle for linear programs," *Operations Research*, vol. 8, no. 1, pp. 101–111, 1960.
- [44] H. Everett, "Generalized lagrange multiplier method for solving problems of optimum allocation of resources," *Operations Research*, vol. 11, no. 3, pp. 399–417, 1963.
- [45] M. Hestenes, "Multiplier and gradient methods," *Journal of Optimization Theory and Applications*, vol. 4, no. 5, pp. 303–320, 1969.
- [46] M. Powell, *A Method for Nonlinear Constraints in Minimization Problems*,. Academic Press, London, ed. r. fletcher ed., 1969.
- [47] R. Glowinski and A. Marocco, "Sur l'approximation, par éléments finis d'ordre un, et la résolution, par pénalisation-dualité d'une classe de problèmes de dirichlet non linéaires," *Revue française d'automatique*, vol. 9, no. 2, pp. 41–76, 1972.
- [48] D. Gabay and B. Mercier, "A dual algorithm for the solution of nonlinear variational problems via finite element approximation," *Computers and Mathematics with Applications*, vol. 2, no. 1, pp. 17 – 40, 1976.
- [49] R. Glowinski and A. Marrocco, "On the solution of a class of non-linear dirichlet problems by a penalty-duality method and finite element of order one," in *Optimization Techniques* (G. I. Marchuk, ed.), Lecture Notes in Computer Science, pp. 327–333, Springer - Verlag, 1974.
- [50] G. H. Golub and C. F. Van Loan, *Matrix Computations (3rd Ed.)*. Baltimore, MD, USA: Johns Hopkins University Press, 1996.
- [51] S. Boyd, N. Parikh, E. Chu, B. Peleato, and J. Eckstein, "Distributed optimization and statistical learning via the alternating direction method of multipliers," *Found. Trends Mach. Learn.*, vol. 3, pp. 1–122, Jan. 2011.
- [52] L. A. Carvalho, "A simple and effective algorithm for detection of arbitrary Hartmann–Shack patterns," *Journal of Biomedical Informatics*, vol. 37, no. 1, pp. 1 – 9, 2004.
- [53] K. Hinnen, M. Verhaegen, and N. Doelman, "Exploiting the spatio-temporal correlation in adaptive optics using data driven H₂-optimal control," *Journal of the Optical Society of America A*, vol. 24, no. 5, pp. 1714–1725, 2007.
- [54] J. Goodman, *Introduction to Fourier Optics, 3rd Ed.* Roberts and Company Publishers, 2005.
- [55] D. Voelz, *Computational Fourier Optics*. SPIE Press, 2011.
- [56] D. Malacara and W. T. Welford, *Optical shop testing*. John Wiley Sons, Inc., 2006.
- [57] E. Candès, "Compressive sampling," in *European Mathematical Society, Proceedings of the International Congress of Mathematicians*, 2006.
- [58] H. Ohlsson, V. Kutchoukov, F. Bociort, S. Pereira, and H. Urbach, "An extension of compressive sensing to the phase retrieval problem," in *Advances in Neural Information Processing Systems*, 2012.

-
- [59] J. Silva, E. Brunner, M. Verhaegen, A. Polo, and C. Visser, “Wavefront reconstruction using intensity measurements for real-time adaptive optics,” in *ECC 2014*, 2013.
 - [60] R. L. Raffard, C. J. Tomlin, and S. P. Boyd, “Distributed optimization for cooperative agents: Application to formation flight,” in *In Proceedings of the 43rd IEEE Conference on Decision and Control*, 2004.
 - [61] O. Manneberg, “Design and simulation of a high spatial resolution Hartmann-Shack wavefront sensor,” Master’s thesis, KTH Stockholm, 2005.
 - [62] J. D. Schmidt, *Numerical Simulation of Optical Wave Propagation With Examples in MATLAB (SPIE Press Monograph Vol. PM199)*. SPIE Press, Aug. 2010.

Glossary

List of Acronyms

MVM	Matrix Vector Multiply
AO	Adaptive Optics
SH	Shack-Hartmann
WFR	Wavefront Reconstruction
DM	Deformable Mirror
E-ELT	European Extremely Large Telescope
EUVL	Extreme Ultra-violet Lithography
CCD	Charge-Coupled Device
FRiM	Fractal Iterative Method
CuRe	Cumulative Reconstructor
SABRE	Spline based Aberration Reconstruction
FFT	Fast Fourier Transform
SPD	Semi Positive Definite
ADMM	Alternate Direction Method of Multipliers

